Supplementary Materials for

Radical-Omics Reveals the Hydrogen-Abstraction Pathway of Isoprene Oxidation

Huan Song[1†‡], Hongyang Cui[2†], Huabin Dong[1†], Ce Chen[1, 2†], Wenyu Wei[1], Yang Li[1], Qindan Zhu[3], Bo Tang[4], Chongqin Zhu[4], Xuefei Ma[1], Zhaofeng Tan[1], Shiyi Chen[1], Yi Wan[2*]& Keding Lu[1*]

Affiliations:

[1]College of Environmental Sciences and Engineering, Peking University, Beijing, China

[2] Laboratory for Earth Surface Processes, College of Urban and Environmental Science, Peking University, Beijing, China

[3]Department of Earth, Atmospheric, and Planetary Science, Massachusetts Institute of Technology, Cambridge, MA 02139, USA

[4]College of Chemistry, Beijing Normal University, Beijing, China

[*]Corresponding authors. Email: wany@urban.pku.edu.cn; k.lu@pku.edu.cn

† These authors contributed equally to this work

[‡] Present address: Department of Atmospheric and Climate Science, University of Washington, Seattle, WA 98195, USA

The PDF file includes:

Materials and Methods

Figs. S1 to S23

Tables S1 to S6

Synthetic Procedures and Characterization Data and Figs. S24 to S28

Table of content

S1. Materials and Methods

S1.1 Chemicals and Reagents

Methanol and acetonitrile (LC/MS grade) were obtained from Merck (Darmstadt, Germany). Milli-Q water was obtained by a Milli-Q water purification system (Millipore, USA). 5,5-Dimethyl-1-pyrroline N-oxide (DMPO) was obtained Aladdin (Shanghai, China). 2,2,6,6-Tetramethylpiperidoxyl (TEMPO) was obtain from Merck (Darmstadt, Germany). CHANT was obtained via the same synthetic procedure referring to Williams, et al. [70]. The high purified nitrogen (99.9999%) cylinders were purchased from AIR LIQUIDE SINGAPORE PTE LTD), isoprene cylinders (500 ppm) were purchased from National Institute of Metrology, China. 1-OH Ta, 1-OH Tb, 4-OH Ta, 4-OH Tb, structure 7, structure 10, structure 11, and DMPO-C_5H_7 was synthesized according to Supplementary Information S4. Standards of the above synthesized chemicals were prepared in MeOH for mass spectrometry imaging (MSI) analysis.

S1.2 Setup of Radical Generation and Capture Equipment

S1.2.1 Custom-build Calibration Source

A laboratory-fabricated calibration source for OH radicals was constructed, employing water vapor photolysis at 185 nm. The calibration system consists of a flow tube (length: 350 mm, inner diameter: ~17 mm) and a lamp module (Fig. S22). To minimize radical loss, the flow tube was coated with a silanization treatment (SilcoNert®, SilcoTek). The flow tube was designed to maintain laminar flow, ensuring a near-parabolic velocity profile and allowing radicals to achieve fully developed flow before entering the photolysis region. Typically, a parabolic velocity profile is characteristic of laminar flow at a rate of 20 L/min. Based on the tube's inner diameter and the

inlet flow rate, the Reynolds number was calculated as 1659.7, confirming a laminar flow regime with a central flow and thinner boundary layers [71,72].

The UV light was provided by a low-pressure mercury discharge lamp (81-1025-01, BHK). A narrow-bandpass filter (185 nm, FWHM = 27.5 nm) was installed in the optical path to ensure that only the relevant photolysis radiation reached the photodetector. Water vapor concentration was adjusted via a dryer, and the mixing ratio of humid air was precisely regulated using a mass flow controller. Humidification of gas flow was achieved by passing the gas through a wash bottle filled with ultrapure water. The humidity of the mixed air was measured using a dew point hygrometer (HL-NT3-D, Rotronic).

The concentration of OH radical generated in the calibration source can be calculated by measuring the effective absorption cross-section of O_2 (σ_{O_2}) and the concentration of O_3 following this equation [73]:

$$[OH]=[HO_2]=[O_3]\cdot\frac{[H_2O]\sigma_{water}}{2[O_2]\sigma_{O_2}} \quad \text{(Eq. S1)}$$

Here, σ_{water} refers to the absorption cross-section of water (7.14×10^{-20} cm²) [74,75]. To minimize the influence of oxygen on the concentration of R• and RO• radicals, we applied extremely low O_2 concentrations in all experiments. Under these conditions, both box model calculations and actual measurements indicated that the O_3 concentration was below the detection limit ($<2.87\times10^{-3}$ppt). With the aid of a stable laser equipment, we first measured the ozone concentration to determine the OH concentration at 6.75% O_2. Simultaneously, the signal intensity of OH (denoted as $[OH]_{count}$) was recorded. Subsequently, we measured OH concentrations and recorded $[OH]_{count}$ under varying relative humidity and flow rates to establish their correlation, which was found to

be linear. This linear relationship allowed us to subsequently determine OH concentrations under low O_2 conditions (<0.1 ppm) directly from the $[OH]_{count}$ signal, without the need for further ozone measurements.

The junction between the calibration source and the solid phase column inlet is a 1/2 Teflon connection (Swagelok). We assume the inner wall of the cylindrical junction as very reactive towards the trace gas because of the collision loss of gas and wall due to the diameter changes. The wall loss rates inside the calibration source (k_{wall1}) and at the junction between the calibration source and the solid phase column inlet (k_{wall2}) can be calculated using Eq. S2 and Eq. S3, respectively [76-78].

$$k_{wall1}=\frac{A}{V}\times\frac{2}{\pi}\times\sqrt{k_e D_g} \quad \text{(Eq. S2)}$$

$$k_{wall2}=3.66\times\frac{D_g}{r^2} \quad \text{(Eq. S3)}$$

Where $\frac{A}{V}$ is the surface-area-to-volume ratio of calibration source equaling to 2.35 cm^{-1}; k_e is the eddy diffusion coefficient of 0.0042 s^{-1} [79]; D_g is the diffusion coefficient; r is the inner diameter of the solid phase column inlet as 0.953 cm. The mean residence times inside the calibration source and, in the junction part, are 0.10 s and 0.02 s, respectively. The total wall loss of radicals needs to be corrected in the calculations. The wall loss rates and fractions of different species are shown in Table S3.

Table S5 summarizes the relative uncertainties associated with the calibration-derived radical concentrations. These uncertainties mainly arise from measurement errors, instrument characteristics, and literature values. By propagating each individual uncertainty using Gaussian

error propagation, the total uncertainty in the calculated radical concentration for this system is determined to be 6.67%.

S1.2.2 Potential Aerosol Mass-Oxidation Flow Reactor (PAM-OFR)

Experiments were also performed in a commercial Potential Aerosol Mass-Oxidation Flow Reactor (PAM-OFR, Aerodyne Research, Inc., Billerica, Massachusetts, USA, hereafter referred to as OFR). In this study, the OH OFR mode was used to investigate the oxidant of isoprene in the absence of NOx at room temperature (T = 298 ± 1 K) and ambient pressure (P = 1003 ± 2 mbar) under the laminar flow condition. Isoprene at a flow rate of 20 mL min^{-1} was mixed into the humid synthetic air at a flow rate of 10 L min^{-1} before entering the OFR.

The total volume of the OFR is 13.3 L, and it consists of four low-pressure-Hg-lamp. High concentrations of oxidants (OH and O_3) can be produced instantly by photolyzing O_3 and O_2, and achieve hours to days of comparative photochemical aging in only minutes of actual time [80]. By utilizing different mercury lamp wavelengths, three distinct OFR modes can be achieved: OFR254, OFR185, and O_3 OFR. O_3 was produced from the irradiation of O_2 with a mercury lamp (λ = 185 nm) and was measured with an O_3 monitor (Thermo Scientific model 49i, USA). Excited oxygen O^1D atoms are produced from UV photolysis of O_3 (λ = 254 nm) inside the OFR. The radical O^1D then reacts with water vapor (introduced using a Nafion membrane humidifier; Perma Pure LLC) to produce OH radicals in the flow tubes. Both O_3 and OH will oxidize organic species. OH exposures were obtained by measuring the decay of SO_2 due to reaction with OH at specific UV lamp intensities and O_3 concentrations. First, SO_2 was introduced with the lamps turned off until its initial concentration ($SO_{2,i}$) remained constant at steady-state conditions. Then, the flow tube and UV lamps were turned on and adjusted to a specific intensity. This condition was maintained

until the final SO_2 concentration ($SO_{2,f}$) at the OFR outlet remained constant. Then, this procedure was repeated at several different conditions to obtain an OH exposure calibration. The OH exposure at each condition is calculated using Eq. S4:

$$OH_{exp} = \frac{1}{k_{OH+SO_2}} \times \ln\left(\frac{SO_{2,i}}{SO_{2,f}}\right) \quad \text{(Eq. S4)}$$

where $k_{OH+SO2} = 9 \times 10^{-13}$ cm^3 $molec^{-1}$ is the bimolecular rate constant between OH and SO_2 [81]. Equation S4 is the result of integrating the differential rate equation for SO_2 and assuming pseudo-first order kinetics. Using this type of calibration procedure has two advantages. First, any potential bias resulting from SO_2 wall losses cancels out. Second, no assumptions about SO_2 residence times need to be made, since the OH exposure (product of the OH concentration and average residence time) is determined directly from the initial and final SO_2 concentrations.

We used OFR185 mode in the experiments of mixed total 200 ppb 111 VOCs oxidation with the resident time of 40s at a relative humidity of 6% (±1%), with the carrier gas as zero air. Typical OH exposure was about 2.6×10^9. Assuming an average atmospheric OH concentration of 1.5×10^6 molec cm^{-3} [82], this experimental exposure is equivalent to 0.68 hour (about 40 mins) of atmospheric oxidation which is typically the lower limit of VOCs' lifetimes. Based on the measured OH exposure and modeling calculation [80], OH radical was always the principal oxidant except for α-pinene, which is 48% comparable to ambient value.

We used OFR185 mode in the experiments involving 500 ppb isoprene alone with liquid N_2 as the carrier gas to produce high concentration of OH radical to avoid the influence of ozone. The resident time is 80s, and the relative humidity is 15%. Typical OH exposure was about 1.5×10^9, which is equivalent to 0.38 hour (about 22 mins) of atmospheric oxidation.

The wall loss of RO_2 radicals in the reaction system consists of two parts: one is inside the OFR and the other is at the junction of the OFR and the solid phase column inlet, both of which can be viewed as first-order reactions. The wall loss rates inside the OFR (k_{wall1}) and at the junction between the OFR and the solid phase column inlet (k_{wall2}) can be calculated using Eq. S2 and Eq. S3, respectively [76-78]. The parameter $\frac{A}{V}$ is the surface-area-to-volume ratio of OFR equaling to 25 m^{-1}; k_e is the eddy diffusion coefficient of 0.0042 s^{-1} [79]; D_g is the diffusion coefficient; r is the inner diameter of the solid phase column inlet as 0.953 cm. The mean residence times inside the OFR and in the junction part are 40s, 80 s and 0.02 s, respectively. The wall loss rates and fractions of different species are shown in Table S4.

S1.2.3 Experiment Settings of radical-omics method

Oxidation of isoprene was selected as a proof-of-principle model in the system. The oxidation reactions were conducted either in the custom-built calibration source or in the OFR, both maintained at controlled ambient temperature (~28 °C), pressure, and relative humidity (ranging from 5% to 60%). High-purity nitrogen served as the carrier gas, further purified through a dedicated deoxygenation system to ensure a low-oxygen environment. Given the total experimental gas flow rate of 20 L/min, eight Gas Clean Oxygen Filter tubes (YJ-O100) were employed in parallel to maintain efficient oxygen removal, accounting for the influence of high flow rates on deoxygenation efficiency. Each filter consists of an acrylic outer shell, a glass inner sleeve, a palladium/manganese oxide deoxidizing agent, and stainless-steel connectors. The internal dimensions are 4 cm in diameter, 28 cm in length, and 351.86 cm^3 in volume, with a maximum flow rate of 5 L/min. The filters achieve residual oxygen concentrations below 0.1 ppm under ambient conditions when treating nitrogen with an initial O_2 content below 1 ppm and at

flow rates under 5 L/min. As confirmed in SI Section S1.2.4, the oxygen concentration in the gas stream was maintained below 0.1 ppm. The UV lamp used for OH radical production was stabilized for at least 30 minutes under a continuous flow of high-purity nitrogen. Simultaneously, purified water in a bubbler was purged with high-purity nitrogen at 5 L/min for at least 30 minutes to efficiently remove dissolved oxygen. This setup ensured sufficiently short residence times and low O_2 concentrations for effective gas-phase radical trapping. After deoxygenation, isoprene was introduced into the system and maintained at 0.5 ppm, providing an excess reactant for OH oxidation.

A solid-phase column was connected to the oxidation system via a 1/2-inch Teflon connector (Swagelok) to capture the generated radicals. Within the column, purified trapping agents—DMPO, TEMPO, or CHANT, as described in Section S1.2.6—were non-covalently bound to a solid polymer matrix, ensuring high sampling efficiency. To prevent photolysis of the trapped radicals and other side reactions, the column was completely wrapped in aluminum foil. For consistency in sensitivity and stability of the trapping reactions across experimental runs, the column temperature was maintained at 30 °C using a precision-controlled spiral heating tape. In the photolysis region of the calibration source, isoprene underwent oxidation, generating reactive radicals within ~0.011 seconds. These intermediates subsequently reacted through inter- and intramolecular pathways in the dark for an additional ~0.109 seconds before being efficiently captured by the solid-phase trapping agents. After sample collection, 5 mL of methanol was used to elute the trapped radicals from the column. A 40 μL aliquot of the eluate was analyzed by UHPLC-Orbitrap-MS (Thermo Fisher Scientific, Bridgewater, NJ, USA) and subsequently quantified by UPLC-MS/MS (Waters, Milford, USA), according to the procedures outlined in Section S1.3.

The absolute concentrations of the target adduct in the elution could be calculated via the comparison with the relative synthetic standard samples. After that, we could calculate the gas phase concentrations of $\cdot C_5H_8(OH)$ and $\cdot C_5H_7$ radicals by the following equation:

$$[\text{Radical}_g]=[C_l]\bullet\frac{[V_e]RT}{PM_rV_s} \quad \text{(Eq. S5)}$$

where $[\text{Radical}_g]$ is the concentration of radical in the gas phase; $[C_l]$ is the captured compounds concentration in the elution; $[V_e]$ is the volume of the elution as 5 mL; R is the gas constant; T is the temperature; P is the pressure, M_r is the molecular mass of the captured compound, for TEMPO-$C_5H_8(OH)$ as 241.275 and DMPO-C_5H_7 as 181.147; V_s is the total volume of sample gas flow.

S1.2.4 Detection of the Oxygen Concentration

The oxygen concentration in nitrogen gas, both from the original cylinder and after deoxygenation, was measured using a gas chromatograph equipped with a plasma emission detector (PED) (LDetek, Canada). During measurement of the nitrogen passing through the deoxygenation tube, the flow rate was set at 2 L/min to match experimental conditions, and a three-way valve was used to divert gas for oxygen detection. Measurements were performed with the Multidetek2 system (LDetek, Canada) using high-purity argon (>99.9999%) as the carrier gas, with a carrier flow rate of 25 mL/min and a sample flow rate of 0.6 mL/min. Gas separation was achieved with a 5A (13×) molecular sieve column. The instrument parameters were as follows: oven 1 temperature, 80 °C; oven 2 temperature, 70 °C; HCD temperature, 45 °C; detector temperature, 60 °C; and analysis time, 300 s. Measurement of the oxygen concentration in nitrogen gas was assisted by the National Institute of Metrology, China. The oxygen concentration in

nitrogen directly from the cylinder was determined to be 0.51 ppm, while the concentration after deoxygenation was below 0.1 ppm.

The oxygen concentration in isoprene was measured using an Agilent 8890 gas chromatograph equipped with a helium ionization detector (Agilent Technologies, Inc., USA). The calibration standard was a primary standard gas (0.993 ppm O_2) from the National Institute of Metrology. The column configuration included: column 1, HP-PlotQ capillary (30 m × 0.32 mm × 20 μm); column 2, MS 5A capillary (30 m × 0.53 mm × 50 μm); columns 3 and 4, Hayesep Q packed columns. The column and detector temperatures were set at 40 °C and 60 °C, respectively. This analysis was supported by Sichuan Zhongce Standard Technology Co., Ltd, China. The measured oxygen concentration in isoprene used for this study was 1.62 ppm. For the experiments, isoprene was introduced at 20 mL/min in a total flow of 20 L/min in the calibration source, and at 20 mL/min in a total flow of 10 L/min in the OFR. In both cases, the total oxygen concentrations were maintained below 0.1 ppm, which was also the value used in the box model simulations.

S1.2.5 Quantification Controls (QCs)

To ensure the correct identification and accurate quantification, strict QCs were implemented in our study. The experiments were carried out in the high-efficiency particulate absorbing (HEPA), positive-pressure, and carbon-filtered clean air lab to minimize blank contamination. All glass equipment was cleaned and rinsed with DCM and n-hexane three times before use. After the preparation of solid phase capture column, the columns were sealed with sealing film (Parafilm®) and secondary seal in a cleaned Ziploc bag. Different concentrations of the synthetic samples were measured and standard curves were plotted in every batch of experiments to correct for variability due to the instrument response.

S1.2.6 The Preparation of Solid-phase Capture Column

Although the purification of commercially purchased DMPO and TEMPO were at high levels (98%), we still detected high impurities of radical adducts possibly formed during their production, which greatly interfered our analysis. Therefore, working standard solutions of DMPO and TEMPO were freshly prepared by HPLC purification process in every batch of experiment. Briefly, 0.2 g DMPO or TEMPO were dissolved in 1 mL loading buffer (Loading buffer was MeOH:H_2O = 1:1). The analytical HPLC system consists of two Shimadzu LC-20AT solvent pumps, an CBM-20Asystem controller, a Prominence SPD-20A diode array detector performing the wavelength scanning from 190 to 400 nm, a manual sample injection valve with a 1 mL loop and an LC Solution workstation for data acquisition and process (Shimadzu, Japan). The samples were separated and analyzed by a reversed phase InertSustain® C18 (250 mm × 4.6 mm i.d., 5 μm, Shimadzu, Kyoto, Japan) column. The mobile phase was consisted of A (water) and B (methanol), which was programmed as follows: 0-3 min, 10% B; 3-30 min, 10-100% B; 30-35 min, 100% B; 35-36 min, 100-10% B; 36-40 min, 10% B. The flow rate was 2 mL/min while the ambient temperature was controlled at 20 °C by air conditioner. The data collection time, sampling interval, response time and pool temperature were 0-36.1 min, 500 msec, 1.0 sec and 40 °C, respectively. For DMPO, the chromatograms were acquired at 270 nm and 275 nm. For TEMPO, the chromatograms were acquired at 450 nm and 435 nm. Then 2 ml of purified DMPO or TEMPO were collected. Finally, the purified DMPO or TEMPO were diluted to 20 mL with water for trapping of radicals.

The radical capture device in this study was capture column, which consisted of a 5 cm 1/2 outer diameter Teflon tube, a 3cm 1/4 outer diameter Teflon tube, a 1/2 to 1/4 turn Teflon tube connector, 80 mg CNW Poly-Sery HLB Pro sorbent (ANPEL Laboratory Technologies (Shanghai) Inc.,

Shanghai, China), and a 6 mL PE frit (ANPEL Laboratory Technologies (Shanghai) Inc., Shanghai, China). The HLB sorbent was filled into a 1/2 outer diameter Teflon tube, with a PE frit attached and tightly sealed with a Teflon tube connector connected to a 1/4 tube. The HLB sorbent was activated with 15 mL MeOH and 15 mL distilled water. The purified capture agent solution (DMPO, TEMPO or CHANT) were loaded on the column, and the sorbents were then dried under gentle nitrogen to remove the water, thus completing the preparation of the capture column.

S1.2.7 Sampling Efficiencies of Capture Column

To evaluate the capture efficiency of the capture column, 750 mg of sorbent was packed and divided into three segments, with each segment analyzed separately to assess sampling efficiency. After radical capture, the column was carefully disassembled to prevent sorbent loss. Trapped radicals were eluted from each segment by adding 5 mL of methanol to the collection vessel. The eluate was filtered using a hydrophobic PTFE needle filter (ANPEL Laboratory Technologies, Shanghai, China) to remove any sorbent particles. A 40 μL aliquot of the filtered solution was then subjected to UHPLC-Orbitrap-MS analysis to determine the capture efficiency of the column. Due to their short life-time and high activity, radicals have already reacted completely before reaching the third segments. Therefore, the third segment was used as a blank. And the capture efficiency (α) was calculated as follow:

$$\alpha = 1 - \frac{C_1}{C_0} = 1 - \frac{1}{m} \quad \text{(Eq. S6)}$$

Where C_0 and C_1 was the concentration of radicals before and after being captured by the sorbent, respectively, the mass spectrum peak area A_1/A_2 was set as m, and A_1 and A_2 was the mass spectrum peak area of captured radicals from the first and second segment, respectively. And for

TEMPO, the efficiency for capturing C_5H_9O, $C_5H_9O_3$, C_5H_7O and $C_5H_7O_2$ was 99.58%, 86.59%, 87.98%, and 100%, respectively. For DMPO, the efficiency for capturing C_5H_9O, $C_5H_9O_3$, C_5H_7, C_5H_7O and $C_5H_7O_2$ was 100%, 100%, 100%, 96.04% and 100%, respectively.

S1.2.8 Kinetic Reactions Between Capture Agents, Oxygen and Radicals

Allylic radicals (U•) such as $•C_5H_8(OH)$ and $•C_5H_7$ in the gas flow react with O_2 and each other to produce further products. In the moment of reaching out with capture agents (T) doped on the filter, competitive reactions occur and therefore the following equations:

$$U\cdot + O_2 \xrightarrow{k_1} UO_2\cdot \quad \text{(R. S1)}$$

$$U\cdot + T\cdot \xrightarrow{k_2} UT \quad \text{(R. S2)}$$

Because of the high concentration of oxygen and capture agents, we can assume they are both quasi-first-order reaction. Thus, after the calculation, we got the concentration of adducts as:

$$[UT]=[U\cdot]\frac{k_2[T\cdot]}{k_1[O_2]+k_2[T\cdot]}(1-e^{(k_1[O_2]+k_2[T\cdot])t}) \quad \text{(Eq. S7)}$$

Where the exponential operator is infinitely close to 1 because of the large reaction rate k_1 and k_2 and the excess oxygen and T•. In this condition, the concentration of adducts only relate to the competitive reaction rates of radical with oxygen. The captured concentration of $•C_5H_7$ increased with decreasing residence time (RT) shown in the Fig. S23 further unveiled the higher rate of $•C_5H_7$ with O_2 than $•C_5H_8(OH)$. In the moment of these radicals reached out for the capture agents, lower ratio of $•C_5H_7$ could be captured by TEMPO because of its higher rate with oxygen than $•C_5H_8(OH)$. DMPO and CHANT, on the other hand, although have higher reaction rates with

293 •C_5H_7, their adducts were also detected as lower concentration before the dioxygen producer as
294 shown in Fig. S11.

295 S1.2.9 Nearest Neighbor Simulation (NNS) Method

296 To accurately interpret the experimental results, it was essential to ensure that the measured
297 concentrations of the captured adducts truly reflected their original branching ratios. To evaluate
298 the true branching ratio in the system, we used the explicit isoprene oxidation mechanism [83] to
299 inverse the branching ratio. We then utilized Nearest Neighbor Simulation (NNS) to determine the
300 initial branching ratios of the four isomeric radicals as 1-OH cis, 1-OH trans, 4-OH cis and 4-OH
301 trans. Because of the lack of the other two isomers in the mechanism, we omitted their yield which
302 is smaller than 5%. A total of 9,751 branching ratio scenarios were evaluated by comparing
303 simulated and experimentally measured concentration ratios. The scenario yielding the smallest
304 deviation was identified as the most accurate representation of the initial branching ratios, as
305 shown in Figure S10.

306

307 S1.3. Analysis of Captured Radicals

308 S1.3.1 UPLC-Orbitrap-MS Analysis

309 Nontargeted radical profiling UPLC-HRMS analysis was carried out on an Thermo Vanquish
310 UPLC system coupled with Q-Exactive Plus mass spectrometer (Thermo Fisher Scientific, U.S.A.)
311 equipped with a heated electrospray ionization (HESI) source. An ACQUITY UPLC® CSH™
312 Fluoro-Phenyl column (2.1 × 100 mm, 1.7 μm particle; Waters) and a mobile phase containing (A)
313 MeOH and (B) ultrapure water were also employed, with a flow rate of 0.3 mL min^{-1}, to separate

the substances with extremely similar polarities. The column and sampler temperatures were maintained at 40 °C and 4 °C, respectively. A total of 5 μL of each sample was injected into the column. The gradient elution program was as follows: the A phase remained at 95% for 1 minutes, then linearly decreased from 95% to 66% from 1 to 2 min and was maintained at 66% from 2 to 13 min; then the A phase linearly decreased from 66% to 0% from 13 to 23 min, and after that, the column was re-equilibrated with 95% B for 2 min before the next injection.

The Orbitrap-MS was operated in positive mode (ESI^+). The mass spectra were collected in Full-MS ddMS2 analysis with top five ions from each MS1 scan being selected for MS/MS fragmentation. To further identify the structures, MS/MS spectra were obtained by PRM mode with inclusion list consisted of compounds of interest. MS1 spectra (*m/z* 50-500) were recorded with inclusion list consisted of compounds of interest. MS1 spectra (*m/z* 50-500) were recorded at resolution of 70,000, with a maximum of 1×10^6 ions collected within 100 ms. MS/MS spectra were obtained with an isolation window of 2 *m/z* and the resolution of 17,500. The normalized collisional energy of higher-energy collisional dissociation was set to 10, 30, and 50. The optimized heated ESI source parameters were set as follows: the spray voltages, 3.5 kV; the capillary temperature, 320 °C; the sheath gas flow rate, 40 Arb; the auxiliary gas flow rate, 10 Arb; the auxiliary gas heater temperature, 300 °C; the sweep gas flow rate, 2 Arb; and the S-lens radio frequency (RF) level, 50. Thermo Xcalibur Qual Browser (Thermo Fisher Scientific, USA) was employed for visualization, processing, and interpretation of mass data.

S1.3.2 Non-Targeted Identification of Trapped Radicals

Thermo Xcalibur Qual Browser (Thermo Fisher Scientific, USA) was employed for visualization, processing, and interpretation of mass data. Progenesis QI 2.3 software (Waters,

USA) was employed to perform the chromatographic peak alignment, picking, and normalization. The picked signals were further proceeded with an intensity more than 10 times that of the corresponding peak from the procedural blank. The molecular formulas corresponding to the signals were determined based on ion mass errors lower than 5 ppm. In this study, TEMPO, DMPO and CHANT trapped various radicals to explore its potential application in the identification of radicals. The most abundant fragmentation ions of TEMPO-radical adducts were at m/z of 126.13 or 140.14, which is generated by the loss of TEMPO group from the adduct. Similarly, the most abundant fragmentation ions of DMPO-radical adducts were at m/z of 114.09 or 98.10, generated by the loss of DMPO. The CHANT-radical adducts generated fragmentation ions of m/z 83.09 or 152.11 via loss of its component (C_6H_{11} or $C_9H_{14}ON$ group). Therefore, the characteristic ions of each trapping agents were used in the MS/MS analysis to identify the potential radicals trapped in our system.

S1.3.3 Targeted Identification of Trapped Radicals

To confirm the origin of $[DMPO\text{-}C_5H_7+2H]^+$, and referring to the calculations of Ma, et al. [84], we additionally detected its subsequent oxidation products. including O_2-adduct peroxyl radicals $[DMPO\text{-}C_5H_7O_2+2H]^+$ (m/z=214.14377), cyclized dioxolane radicals $[TEMPO\text{-}C_5H_7O_2+H]^+$ (m/z=256.19072), alkoxyl radicals $[DMPO\text{-}C_5H_7O+2H]^+$ (m/z=256.19072), a possible oxetane-substituted methyl radicals $[TEMPO\text{-}C_5H_7O+H]^+$ (m/z=240.1958), its O_2-adduct peroxyl radicals $[DMPO\text{-}C_5H_7O_3+2H]^+$ (m/z= 230.13868), and the allylic radicals formed after peroxyl radicals' H-shift reaction $[TEMPO\text{-}C_5H_7O_3+H]^+$ (m/z=272.18563). All these products were further infused into the HESI- Orbitrap-MS in a positive ion mode to explore their fragmentation. The molecular mass of $[DMPO\text{-}C_5H_7O_2+2H]^+$ were found as precursor ions, and regular and intense product ions with 55.06, 114.09, 214.14 were observed. Similarly, the molecular mass of $[DMPO\text{-}C_5H_7O+2H]$

359 $^{+}$ were found as precursor ions, and regular and intense product ions with 81.07, 98.10, 198.15
360 were observed. The product ion of 98.10 and 114.09 were considered to cause a loss of DMPO in
361 the DMPO trapped radicals. Compound [TEMPO-$C_5H_7O_2$+H] $^{+}$ and [TEMPO-C_5H_7O+H] $^{+}$ were
362 also found as precursor ions, respectively. The product ion of 126.13 was derived from the TEMPO
363 of the TEMPO trapped radicals. The identification of these oxidation products further supports our
364 assignment of the peak at retention time 5.77 min as the captured •C_5H_7 radical. The products from
365 •C_5H_7 follow the similar line of •C_5H_9O oxidation. Peroxyl radical $C_5H_7O_2$• produces cyclized
366 dioxolane radical and alkoxyl radical under no NOx condition. Alkoxyl radical undergoes
367 cyclization [85] reaction to oxetane-substituted methyl radical. Visible ratio of C_5H_7O• to $C_5H_7O_2$•
368 under no NOx condition indicated the possibility of a new reaction pathway involving the
369 generation of RO• radicals, and followed by rapid 1,5-HAT, β-scission, or cyclization, potentially
370 leading to R• radical formation in the atmosphere. What's more, in the line of •C_5H_7 oxidation, the
371 cyclization pathway do not fully align with the •C_5H_9O oxidation, suggesting that additional
372 reaction pathways may generate new products contributing to secondary organic aerosol (SOA)
373 formation, particularly in environments where highly oxygenated molecules (HOMs) or IEPOX-
374 like products may form [84].

375 S1.3.4 UPLC-MS/MS Analysis

376 Targeted quantification of trapped radical analysis was carried out on a ACQUITY UPLC
377 coupled with Xevo TQXS triple quadrupole mass spectrometry (Waters, Milford, USA) equipped
378 with an electrospray ionization (ESI) source. An ACQUITY UPLC® CSH™ Fluoro-Phenyl
379 column (2.1 × 100 mm, 1.7 μm particle; Waters) and a mobile phase containing (A) ultrapure water
380 and (B) MeOH were employed for chromatographic separation, with a flow rate of 0.3 mL min^{-1},
381 to obtain the abundant responses of the targeted trapped radicals. The column and sampler

temperatures were maintained at 35 °C and 8 °C, respectively. A total of 2 μL of each sample was injected into the column. The gradient elution program was as follows: the B phase remained at 5% for 1 minutes, then linearly increased from 5% to 34% from 1 to 4 min and maintained at 34% from 4 to 12 min. Then, the B phase linearly increased from 34% to 100% from 12 to 23 min. After that the column was re-equilibrated with the initial mobile phase composition for 2 min before the next injection.

The MS/MS was operated in positive mode (ESI^+). The mass spectra were collected in multiple-reaction monitoring (MRM) mode. The parameters were set as follow: the capillary voltage, 3 kV; the cone voltage, 30 V; the source offset voltage, 30 V; the source temperature, 150 °C; the desolation temperature, 500 °C; the cone gas flow rate, 1,200 L/Hr; the collision gas flow rate, 0.15 mL/min; the nebulizer gas flow, 7 Bar. The data were obtained and analyzed using MassLynx V4.2 software (Waters, Milford, USA).

S1.3.5 Standard curves of captured compounds

The concentrations of captured radicals were quantified relative to the synthesized standard sample. The synthesized standard samples were diluted with methanol into solutions of different concentrations: six different concentrations of mixed standard solutions of 1-OH Ta and 1-OH Tb between 0.1 ng/mL and 20 ng/mL, six different concentrations of mixed standard solutions of 4-OH Ta and 4-OH Tb between 0.05 ng/mL and 10 ng/mL, and six different concentrations of standard solution of DMPO-C_5H_7 between 0.1 ng/mL and 10 ng/mL. All stock solutions were stored at -80 °C, and a series of diluted solutions were stored at -20 °C. During each mass spectrometry analysis, the same method was used to analyze a series of standard solutions of different concentrations. The concentration of each part in the mixed standard sample was

404 determined based on the average proportion of signal response intensity. Standard curves between
405 signal response intensity and concentrations were obtained from standard solutions of different
406 concentrations. For each experiment, all curves provided adequate linearity ($R^2 > 0.995$). Figure
407 S2 showed the standard curve used in a certain experiment.

408

409 S1.4. Theoretical Methods and Modeling Calculation

410 S1.4.1 Quantum Chemical Calculation.

411 Structures were fully optimized at the UB3LYP-D3/6-31+G(d,p) level of theory. For the
412 isomerization reactions, vibrational frequency calculations were performed to make sure that there
413 is zero (one) imaginary frequency for minimum (transition state) structures. In addition, intrinsic
414 reaction coordinate (IRC) was performed at same level to check the connectivity among reactant,
415 product and transition state. All these calculations were performed using the Gaussian 16 program
416 [86].

417 S1.4.2 Rate Constant Calculations

418 All rate constant calculations k were performed using a Master Equation Solver for Multi
419 Energy-well Reactions (MESMER) code [87]. For the barrierless TEMPO+C_5H_9O reactions,
420 conventional TST and variational TST are not appropriate because the reaction coordinated is not
421 well-defined, a situation which is typical of association reactions between two pen-shell species [88].
422 Therefore, the associated k rate constants for the barrierless bimolecular reactions were evaluated
423 by the Inverse Laplace Transform (ILT) method of the modified Arrhenius form of the

experimental high-pressure association rate coefficient [89]. The general ILT method can be represented in Eq. S7:

$$k^{\infty}(\beta)=A^{\infty}\left(\frac{1}{\beta}\right)^{n^{\infty}}\exp(-\beta E^{\infty}) \quad \text{(Eq. S7)}$$

Where $k^{\infty}(\beta)$ is the high pressure limiting rate coefficient; $\beta=1/kT$; A^{∞} is the preExponential, and n^{∞} is the infinity; T was set to 300K; A^{∞} was set to 6.2×10^{-12} cm^3 $molecule^{-1}$ s^{-1}; E^{∞} and n^{∞} are both set to 0, which are identical to those used previously [90,91]. The input parameters for electronic geometries, vibrational frequencies, and rotational constants were calculated at UB3LYP-D3/6-31+G(d,p) level.

S1.4.3 Box Model Settings

To evaluate the true branching ratio in this no chemical equilibrium system, we used the MCM v3.3.1 isoprene oxidation mechanism to inverse the branching ratio. Given the low oxygen concentration in our study, its impact was accounted for in the correction of KDEC, a generic rate coefficient applied to hydroxyalkoxy species decomposition. Parameters such as temperature, pressure, photolysis time, residence time, and dilution coefficient were input into the kinetic box model.

S1.4.4 CAM-Chem Simulation

We use the Community Earth System Model/Community Atmosphere Model with chemistry version 2.2.0 (CAM-Chem) to investigate the impact of an updated isoprene oxidation mechanism on the global radical budget and secondary organic aerosol (SOA) formation [92,93]. The CAM-Chem simulations are conducted at a horizontal resolution of 1.25° × 0.95° with 32 vertical layers.

Meteorological fields are nudged to the Modern-Era Retrospective Analysis for Research and Applications, Version 2 (MERRA-2). Anthropogenic and biomass burning emissions are consistent with the Coupled Model Intercomparison Project Phase 6 (CMIP6) [94-96]. Biogenic NMVOC emissions are calculated online using the Model of Emissions of Gases and Aerosols from Nature (MEGAN) v2.1[97]. We conduct three simulations using identical emissions but varying chemical mechanisms. The baseline simulation is configured with the MOZART-TS2 mechanism [98]. The second simulation incorporates an updated TS2 mechanism with hydrogen abstraction pathway and the corrected branching ratio of OH addition allylic radical. All simulations results are performed average values for the period 2011–2013.

Beyond SOA precursors discussion in the manuscript, the shift in branching ratios exerts broader impacts on atmospheric oxidative balance. The redistribution of oxidation flux away from IEPOX suppresses one known HO_x recycling pathway associated with IEPOX multiphase processing. As illustrated in Figure S20, model simulations capture regional variations in OH production rates, with decreases over isoprene-rich humid tropics such as the Amazon, Congo Basin, Maritime Continent, and Southeast Asia where IEPOX-driven HO_x recycling is diminished. In contrast, moderate increases appear over subtropical and temperate regions such as East Asia, South Asia, and the southeastern United States, reflecting the net response of the altered oxidation network. While the current model framework does not explicitly resolve potential secondary radical cycling involving H-abstraction-derived products, the chemical structure of these di-carbonyls suggests possible reactivity in both aqueous-phase and multiphase radical networks, potentially contributing additional HO_x regeneration and SOA formation under specific conditions. Further laboratory and mechanistic studies are required to quantify these pathways, particularly under tropical convective conditions. In addition to the spatial responses, global mean diagnostics

indicate that the incorporation of H-abstraction induces limited changes in the global OH concentration (Table S6). However, regional redistribution of isoprene oxidation flux reduces IEPOX while enhancing highly oxygenated intermediates, potentially elevating aqueous SOA formation in susceptible regions.

S2. Figs.S1 to S23

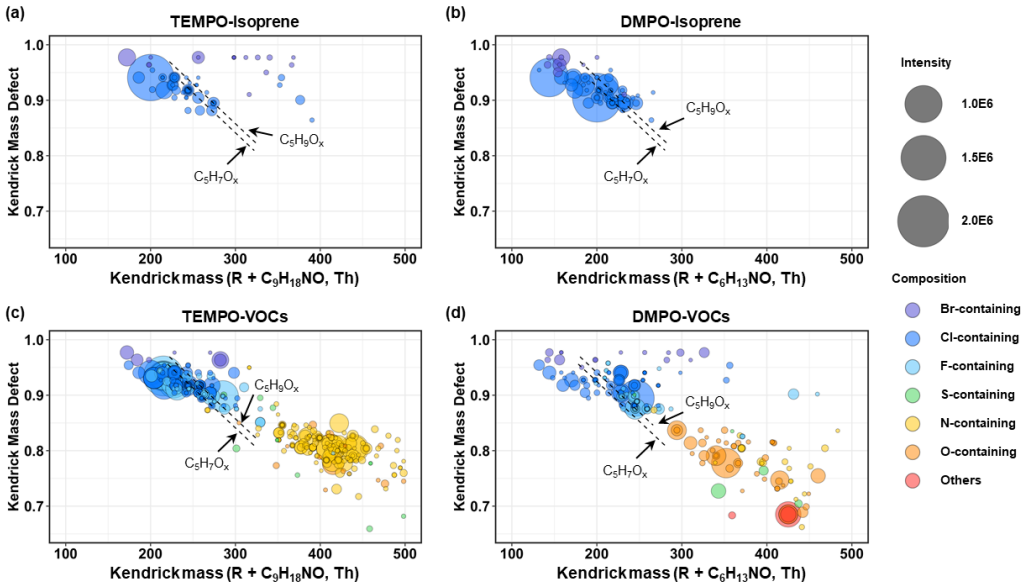

Figure S1. Kendrick mass–defect fingerprints of radical adduct formed during OH oxidation. (a) TEMPO–isoprene; (b) DMPO–isoprene; (c) TEMPO–mixed VOCs; (d) DMPO–mixed VOCs. The x-axis is the Kendrick mass (Th) after adding the trap mass to the radical: R + $C_9H_{18}NO$ for TEMPO and R + $C_6H_{13}NO$ for DMPO. The y-axis is the Kendrick mass defect (KMD). Each circle denotes a uniquely assigned radical adduct (R–TEMPO or R–DMPO). Symbol area scales with ion signal (reference sizes at right: 1.0×10^6, 1.5×10^6, 2.0×10^6 abundance). Colors indicate elemental classes (legend at lower right: Br-, Cl-, F-, S-, N-, O-containing, and others meaning C_xH_y species). Dashed arrows highlight two recurrent homologous families, $C_5H_9O_x$ and $C_5H_7O_x$ (x=0-5). The $C_5H_9O_x$ cluster is consistent with adducts of OH-addition-derived allylic radicals, whereas the $C_5H_7O_x$ cluster indicates hydrogen-abstraction-derived carbon-centered radicals ($\bullet C_5H_7$). The same two trends appear in both single-precursor (isoprene) and mixed-VOC experiments and for both traps, demonstrating methodological consistency and providing a unified, omics-style fingerprint of early-stage radical chemistry.

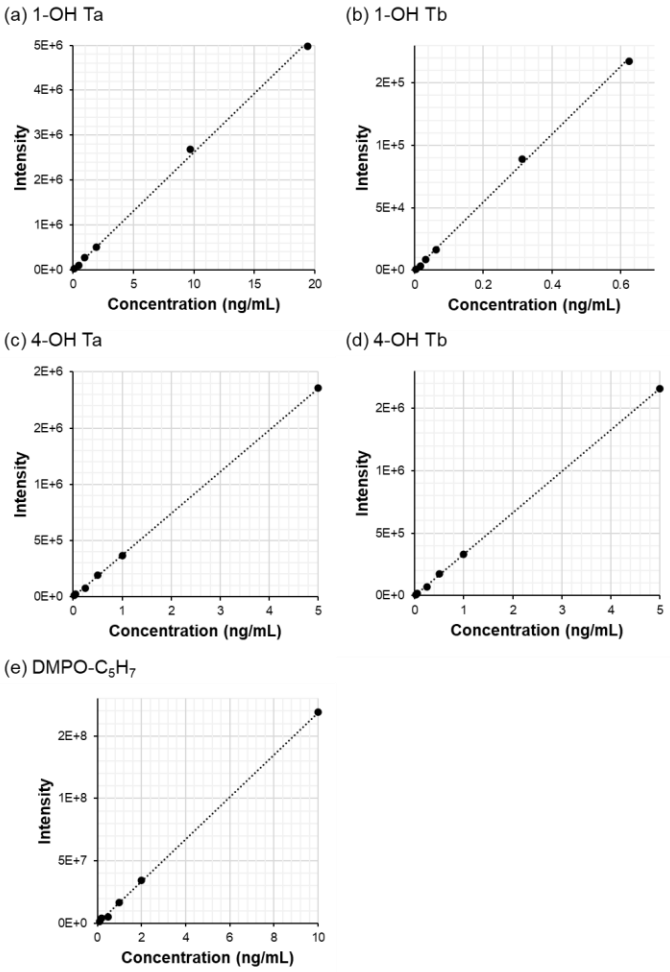

Figure S2. Standard curves of each TEMPO-C_5H_9O and DMPO-C_5H_7 standard samples in a certain experiment. The standard curves were calculated in every batch of experiment, we just showed one of them here. (a) 1-OH Ta: Intensity = 260741 × Concentration (ng/mL) + 14457 (R^2=0.9987). (b) 1-OH Tb: Intensity = 271456 × Concentration (ng/mL) + 116.21 (R^2=0.999). (c) 4-OH Ta: Intensity = 372084 × Concentration (ng/mL) - 3471.1 (R^2=0.9999). (d) 4-OH Tb: Intensity = 332100 × Concentration (ng/mL) - 1738 (R^2=0.9999). (e) DMPO-C_5H_7: Intensity = 16985608 × Concentration (ng/mL) - 541201 (R^2=0.9994). The concentration of 1-OH Tc and 4-OH Tc in sample was calculated according to the standard curves of 1-OH Ta and 4-OH Ta, respectively.

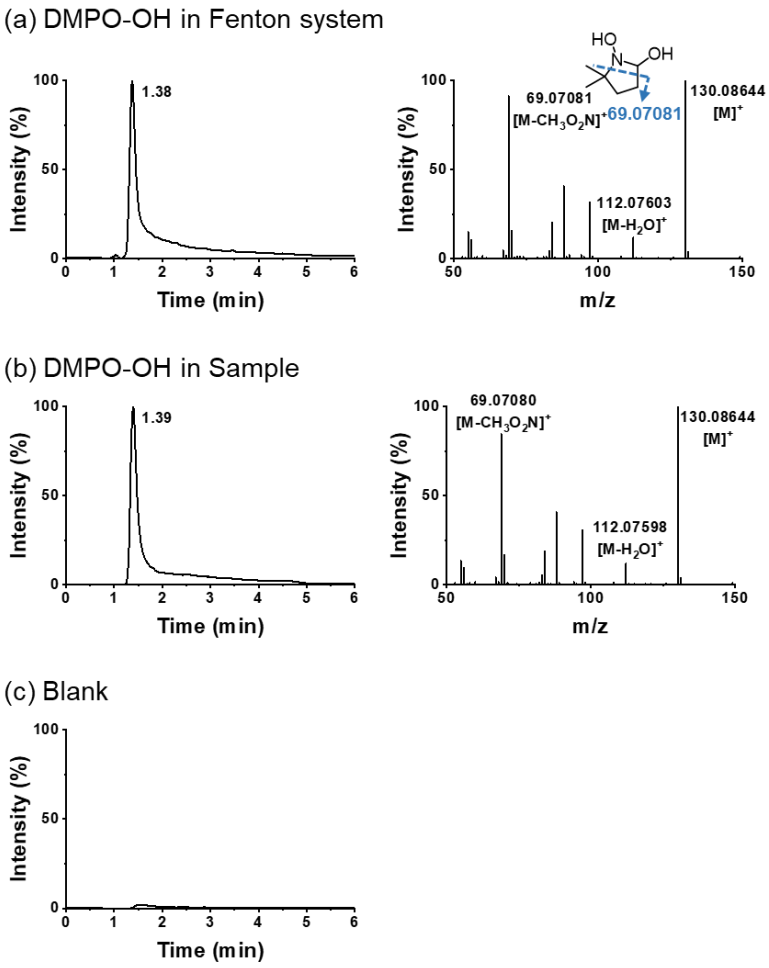

498

499 Figure S3. Radical OH standard in the Fenton-reaction system and the gas phase sample. (a) The
500 peak of DMPO-OH generated through Fenton-reaction system was eluted at 1.38 min. Compared
501 to this standard solution, the characteristic peak was also occurred (b) when using DMPO to
502 capture the products of gas phase isoprene and OH in calibration source. The process blank (c)
503 also indicated this peak was related to DMPO-OH.

504

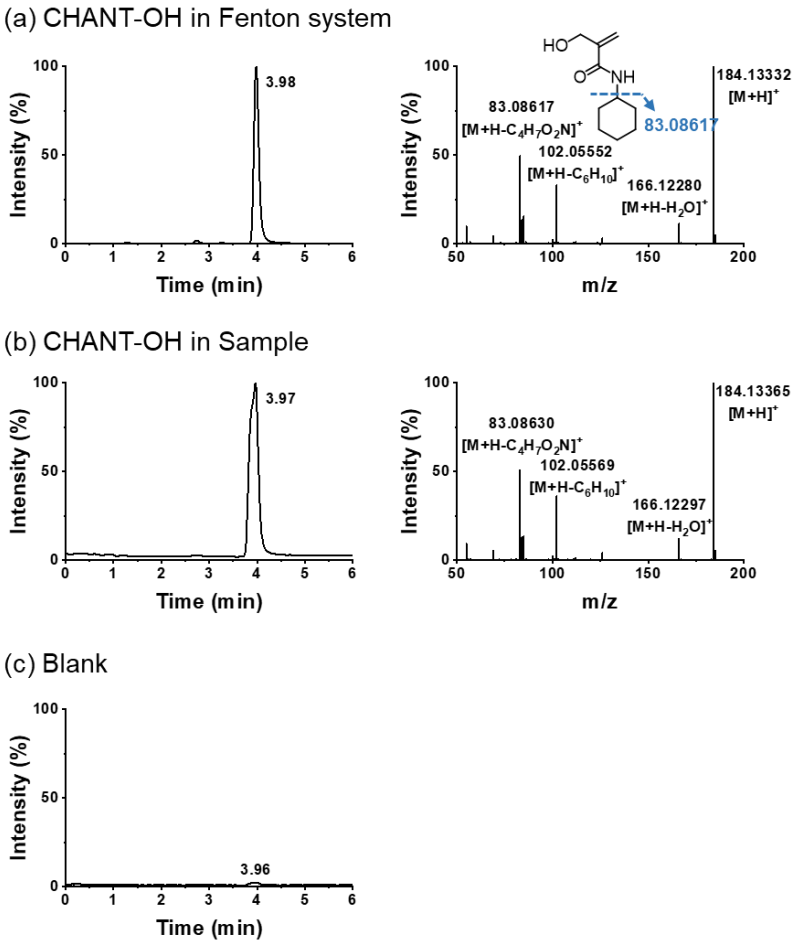

505

506 Figure S4. Radical OH standard in the Fenton-reaction system and the gas phase sample. (a) The
507 peak of CHANT-OH generated through Fenton-reaction system was eluted at 3.98 min. Compared
508 to this standard solution, the characteristic peak was also occurred (b) when using CHANT to
509 capture the products of isoprene and OH in calibration source. The process blank (c) also indicated
510 this peak was related to CHANT-OH.

511

512

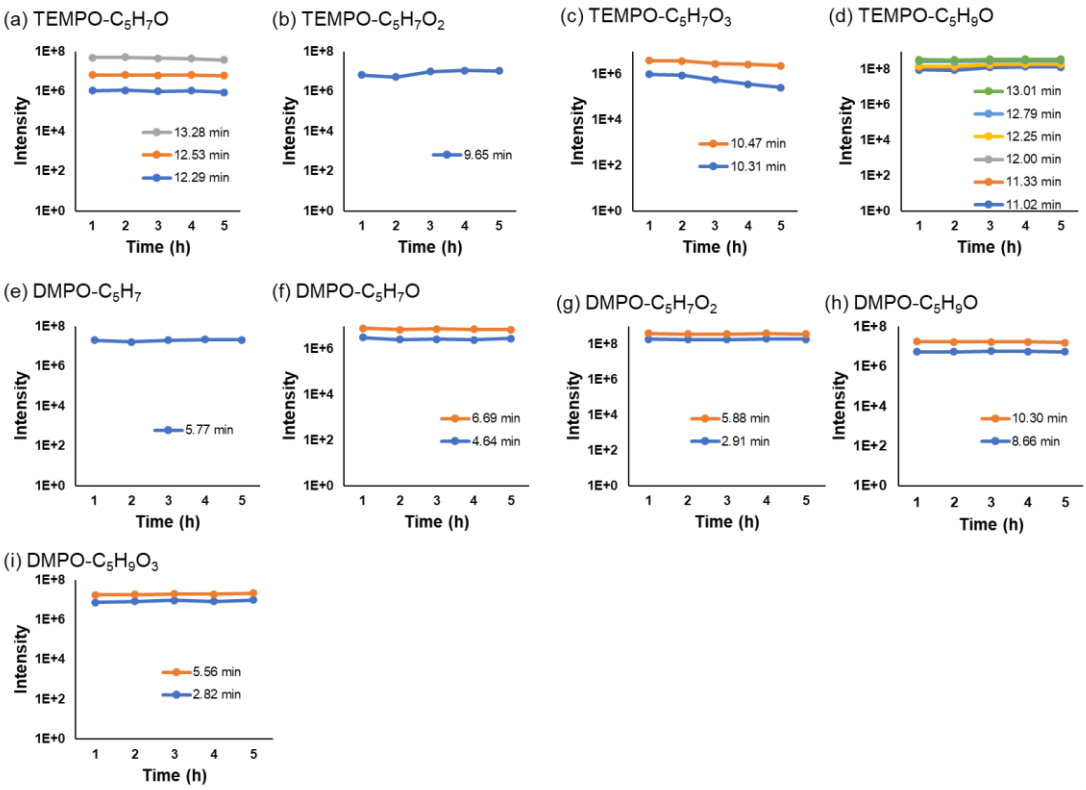

513

514 Figure S5. Stability of the captured compounds after elution. The elution solution was measured

515 through nontargeted UPLC-MS analysis every hour, for a total of five measurements.

516

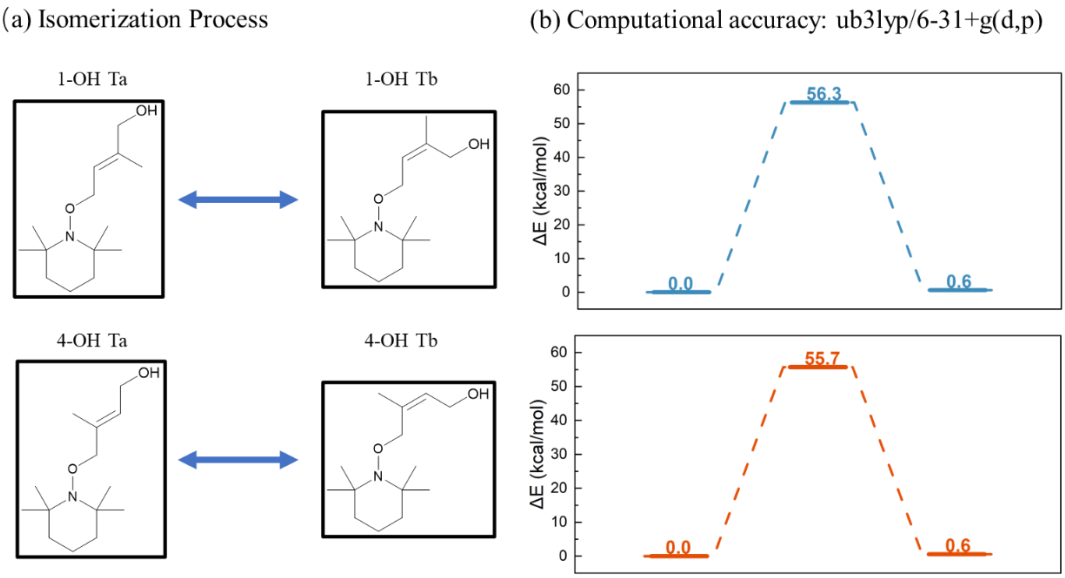

517

518 Figure S6. Structures were fully optimized at the UB3LYP-D3/6-31+G(d,p) level of theory. For
519 the isomerization reactions, vibrational frequency calculations were performed to make sure that
520 there is zero (one) imaginary frequency for minimum (transition state) structures. In addition,
521 intrinsic reaction coordinate (IRC) was performed at same level to check the connectivity among
522 reactant, product and transition state. All these calculations were performed using the Gaussian 16
523 program [86]. There is high energy base, ~55 kcal/mol, structure isomers in the elution would not
524 isomerize.

525

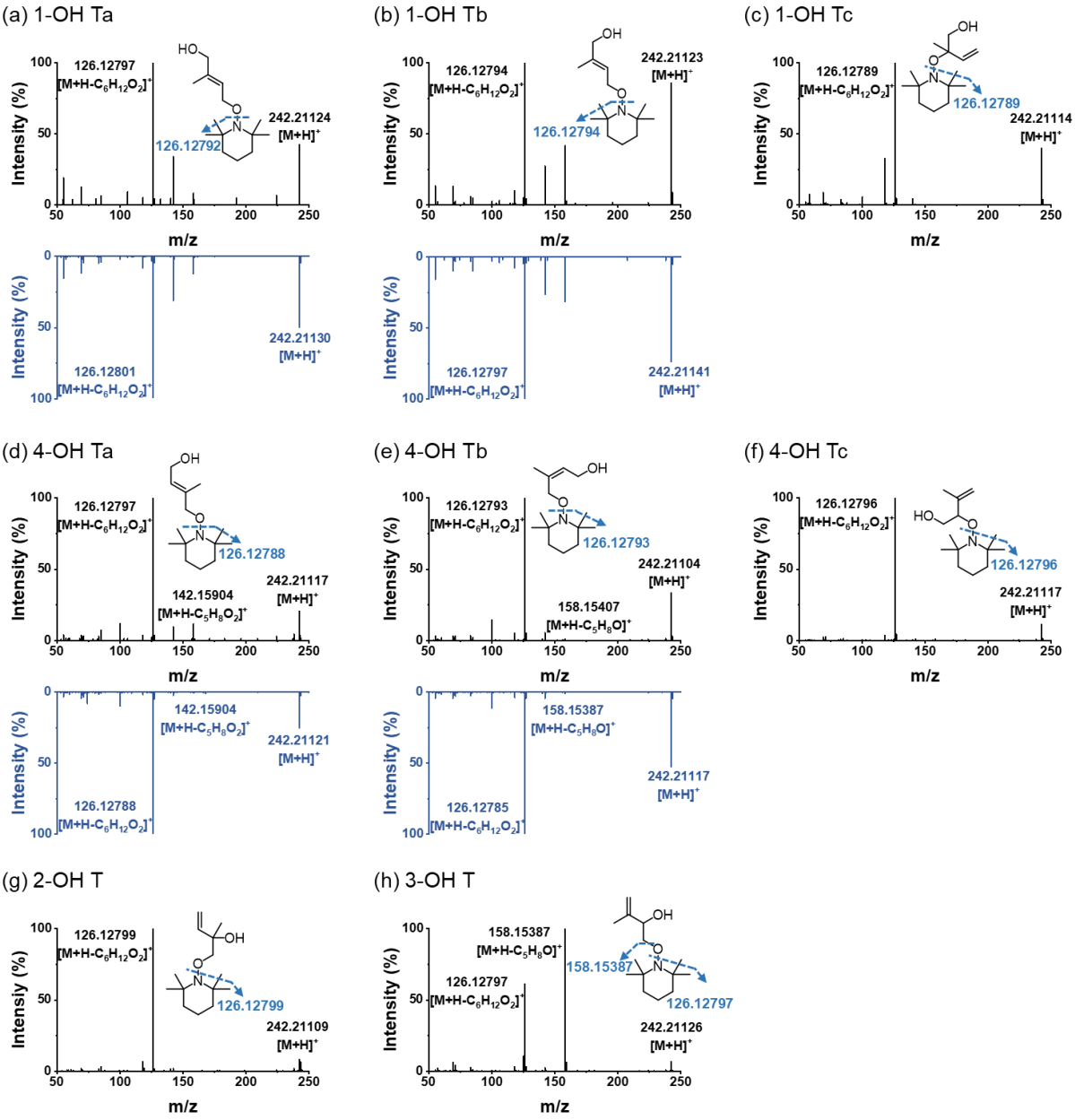

526

527 Figure S7. In order to identify the TEMPO-trapped products of compound C_5H_9O ([TEMPO-
528 C_5H_9O+H] $^+$, m/z = 242.21150), the MS/MS spectrum for each peak was analyzed. No visible
529 signal in the OFR experiments. The relative retention times (RT) of these adducts were further
530 corroborated by their predicted LogP (octanol-water partition coefficient) values. (a-b) The
531 TEMPO-trapped products of 1-OH Ta and 1-OH Tb was compared to the standard sample,

532 respectively. (c) The MS/MS analysis of TEMPO-trapped products of 1-OH Tc. (d-e) The
533 TEMPO-trapped products of 4-OH Ta and 4-OH Tb was compared to the standard sample,
534 respectively. (f-h) The MS/MS analysis of TEMPO-trapped products of 4-OH Tc, 2-OH T, and 3-
535 OH T. The MS/MS analysis revealed that these peaks exhibited precursor ions with the expected
536 molecular masses, along with characteristic product ions at m/z 126.13 and 158.15, corresponding
537 to the loss of the TEMPO from the trapped radical adducts.

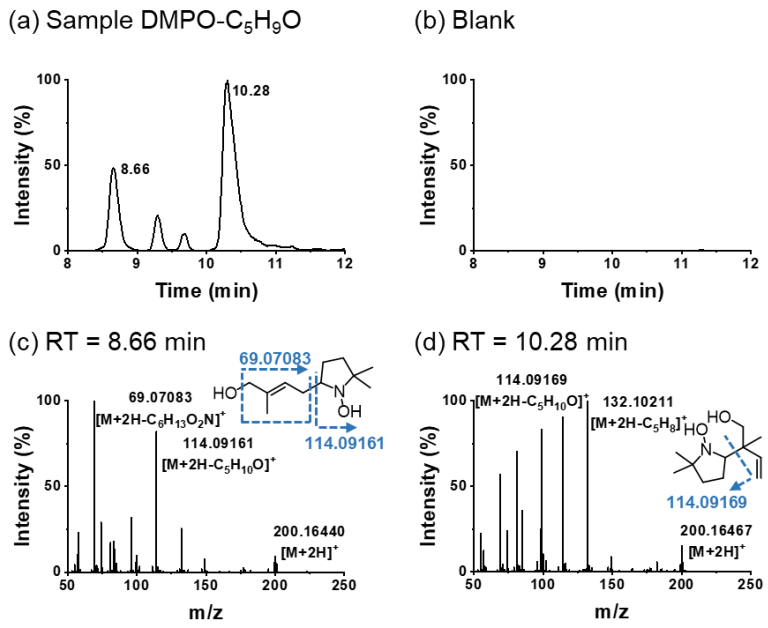

538

539 Figure S8. The DMPO-trapped adducts of C_5H_9O in the experiments of calibration source were
540 analyzed as shown in (a). The $[DMPO\text{-}C_5H_9O+2H]^+$ (m/z = 200.16450) peaks were extracted, and
541 their MS/MS spectra were examined. By comparison with the process blank (b) and based on
542 precursor ion analysis, the peaks at 8.66 and 10.28 min were identified as major DMPO-trapped
543 products. Two possible structures proposed as shown in (c) and (d). The MS/MS spectra displayed
544 a dominant product ion at m/z 114.09, consistent with the dissociation of the DMPO from the
545 radical adduct. All DMPO adducts in this study were analyzed and quantified using the [DMPO-
546 $R+2H]^+$ ion signal. This is because DMPO-derived radical adducts can undergo disproportionation
547 reactions in solution, resulting in the presence of both oxidized ($[M]^+$) and reduced ($[M+2H]^+$)
548 forms. The relative abundance of $[M]^+$ and $[M+2H]^+$ formed by different adducts varies and
549 depends on the type of radical trapped. Moreover, their retention times are also different, indicating
550 that these species are chemically distinct entities already present in solution, rather than simply
551 being products of protonation in the ion source [99]. Previous studies have shown that the proportion
552 of the reduced $[M+2H]^+$ ion increases with the molecular size of the spin adduct, while the

oxidized form ($[M]^+$) is generally only predominant for certain adducts such as DMPO-OH, which typically appears primarily as $[M+H]^+$ in ESI-MS [99,100]. For the C_5H_7 radical adduct, both $[M]^+$ and $[M+2H]^+$ ions were detected; however, the abundance of the $[M]^+$ ion was much lower, accounting for only about 1% of the $[M+2H]^+$ signal. Therefore, to ensure consistency and avoid confusion, only the $[M+2H]^+$ extracted ion chromatograms and mass spectra are shown for all DMPO adducts in this work, except for OH radical.

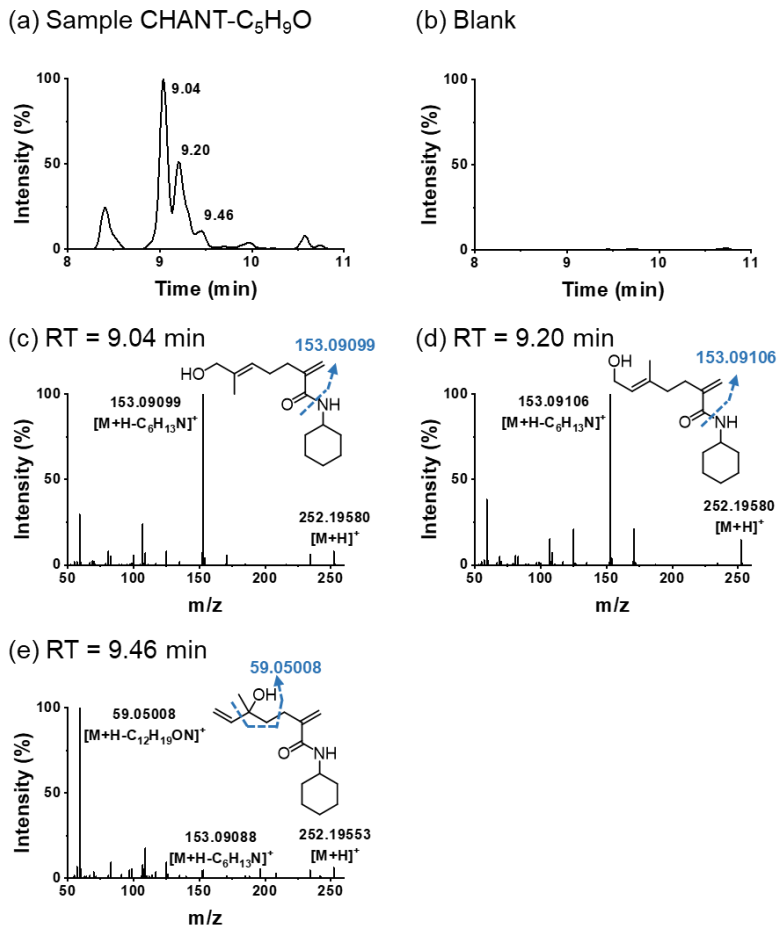

560

561 Figure S9. The CHANT-trapped adducts of C_5H_9O in the experiments of calibration source were
562 analyzed as shown in (a). The [CHANT-C_5H_9O+H] $^+$ (m/z = 252.19580) peaks were extracted,
563 and their MS/MS spectra were examined. By comparison with the process blank (b) and based on
564 precursor ion analysis, the peaks at 9.04, 9.20 and 9.46 min were identified as major CHANT-
565 trapped products. The possible structures proposed as shown in (c), (d) and (e). The MS/MS spectra
566 displayed a dominant product ion at m/z 153.09, consistent with the dissociation of the CHANT
567 from the radical adduct.

568

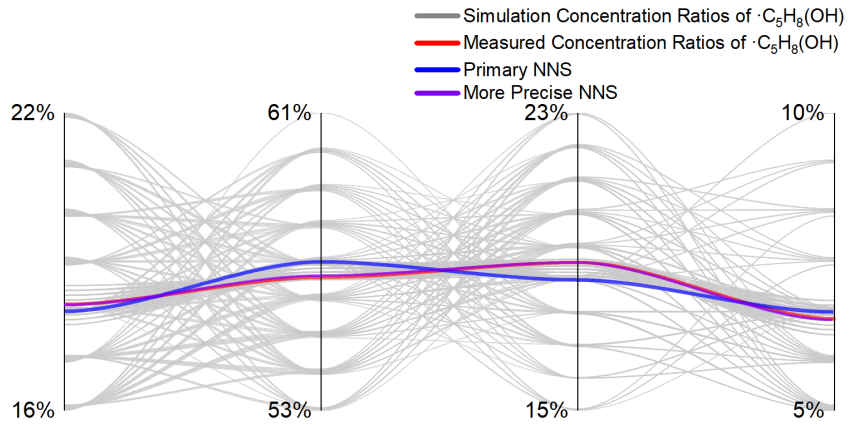

569

570 Figure S10. Based on up to 9751 routines of different branching ratios s of 1-OH trans, 1-OH cis,
571 4-OH trans and 4-OH cis radicals setting calculation, the Nearest Neighbor Search (NNS) of
572 modelled concentrations of •C_5H_8(OH) to measured ones was found at 0.172: 0.509:0.215:0.068.

573

574

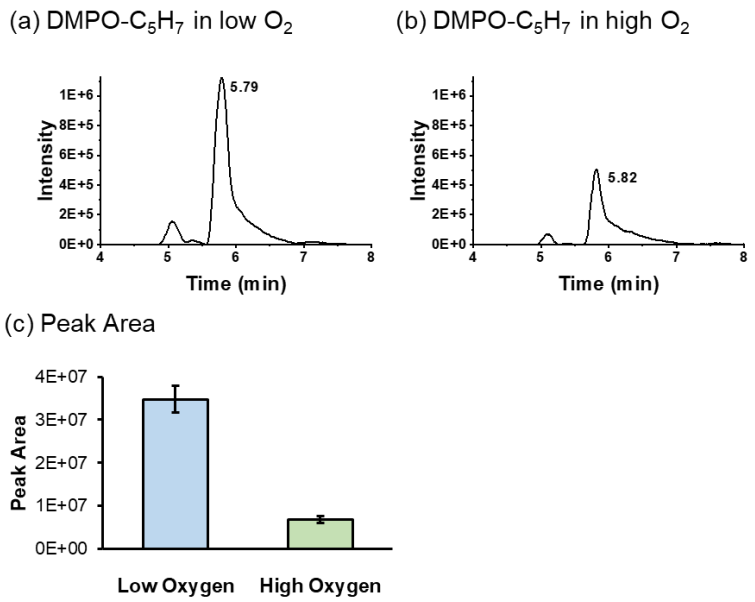

575

576 Figure S11. In order to compare the yield of compound C_5H_7 under (a) low O_2 (under 0.1ppm) and
577 (b) high O_2 (0.51ppm), the characteristic DMPO-C_5H_7 (m/z = 182.15) peaks were extracted
578 respectively. The peak was eluted at (a) 5.79 min and (b) 5.82 was identified as the DMPO-trapped
579 products. (c) The peak areas of the targeted product under different concentration of oxygen were
580 compared.

581

582

583

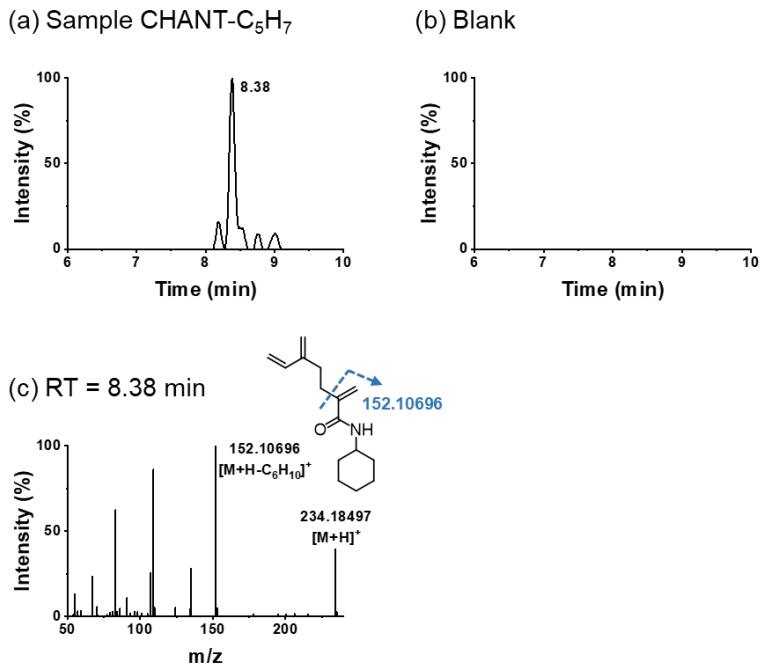

584

585 Figure S12. The CHANT-adducted product of C_5H_7 generated from calibration source was
586 identified through comparison between sample (a) and process blank (b) with isoprene but without
587 uv photolysis. The peak at 8.38 min was identified as $[CHANT\text{-}C_5H_7+H]^+$ (m/z = 234.19). The
588 MS/MS spectra displayed a dominant product ion at m/z 152.10696, consistent with the loss of
589 C_5H_7.

590

591

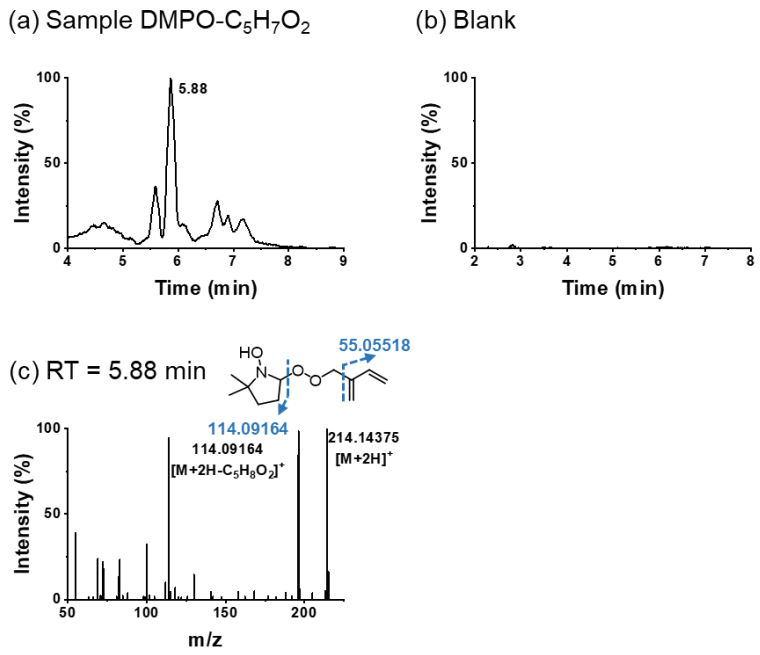

592

593 Figure S13. The DMPO-trapped adducts of $C_5H_7O_2$ generated from calibration source (a) were
594 identified by comparison with process blank (b). The characteristic peaks, corresponding to
595 [DMPO-$C_5H_7O_2$+2H] $^+$ (m/z = 214.14), with retention time of 5.88 min was identified as the
596 DMPO-trapped products. MS/MS analysis of this peak revealed the molecular mass of [DMPO-
597 $C_5H_7O_2$+2H] $^+$ as precursor ions. (c) In the MS/MS spectrum of the peak, regular and intense
598 product ions with 114.09, and 55.06 were observed. The product ion of 114.09 was considered to
599 cause a loss of DMPO in the DMPO trapped radicals. And the product ion of 55.06 was considered
600 as the loss of a butadiene. No visible signals in the experiments from OFR which could be
601 attributed to the prolonged resident time facilitating following reactions.

602

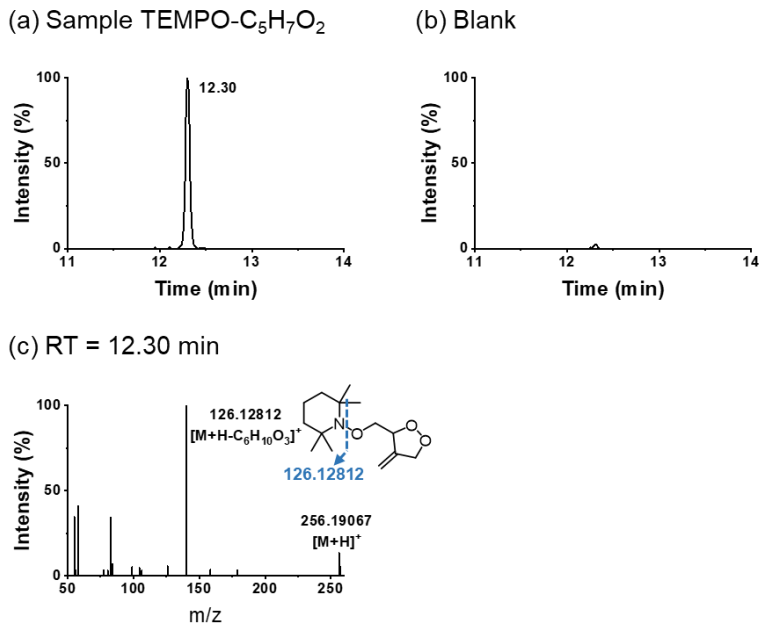

603

604 Figure S14. The TEMPO-adducted product of compound $C_5H_7O_2$ was identified through
605 comparison between sample (a) and process blank (b) in the experiments of OFR. The
606 characteristic [TEMPO-$C_5H_7O_2$+H] $^+$ ion (m/z = 256.19) eluted at 12.30 min and was selected for
607 MS/MS analysis. The fragmentation spectrum exhibited the precursor ion at the expected m/z
608 256.19, along with a dominant product ion at m/z 126.13, corresponding to characteristic TEMPO-
609 derived fragments.

610

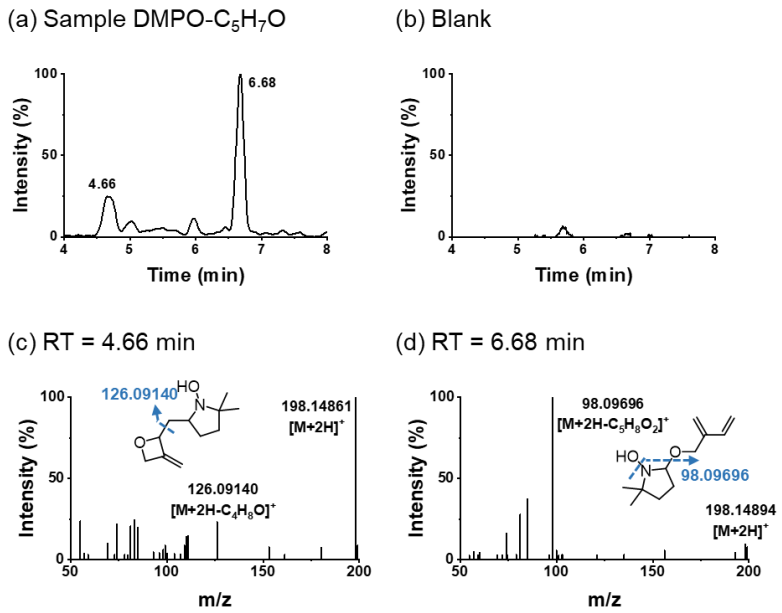

611

612 Figure S15. The DMPO-adducted product of C_5H_7O generated from calibration source was
613 identified through comparison between sample (a) and process blank (b). The characteristic
614 [DMPO-C_5H_7O+2H] $^+$ ion (m/z = 198.15) eluted at 4.66 and 6.68 min and were selected for
615 MS/MS analysis. (c) In the MS/MS spectrum of the first peak, regular and intense product ion with
616 126.09 were observed, which was considered that the DMPO fragmentation in the product lost
617 another hydroxyl group. (d) In the second peak, regular and intense product ion with 98.09 was
618 considered as the DMPO fragmentation of adducts. No visible DMPO-trapped products of
619 compound C_5H_7O were detected in the OFR experiments which could be attributed to the
620 prolonged resident time facilitating following reactions.

621

622

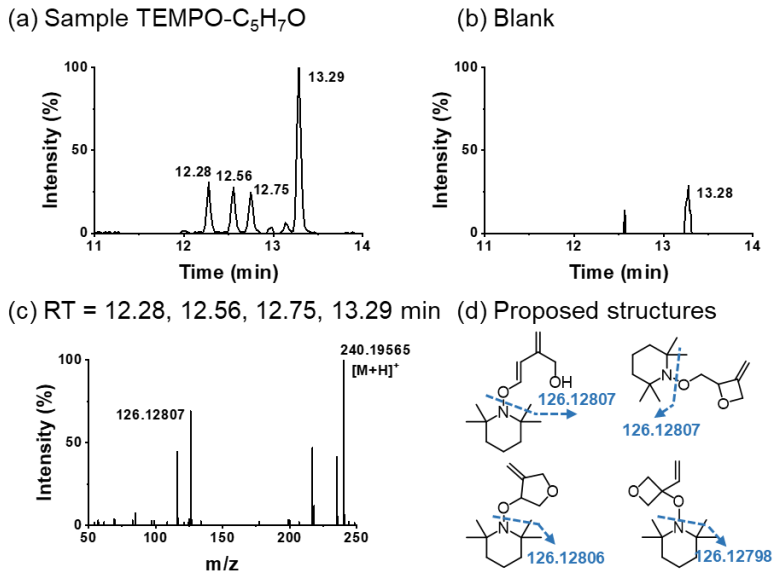

623 Figure S16. The TEMPO-adducted product of compound C_5H_7O generated from calibration
624 source was identified through comparison between sample (a) and process blank (b). The
625 characteristic $[TEMPO\text{-}C_5H_7O+H]^+$ ion (m/z = 240.20) eluted at 12.28, 12.56, 12.75 and 13.29
626 min was selected for MS/MS analysis. MS/MS analysis revealed that these peaks were similar to
627 each other, and the MS/MS analysis of 13.29 was shown in (c). The peak exhibited precursor
628 ions with the expected molecular masses, along with characteristic product ions at m/z 126.13,
629 corresponding to the loss of the TEMPO fragmentation from the trapped radical adducts. (d) The
630 proposed structures for $TEMPO\text{-}C_5H_7O$. No visible signals in the experiments from OFR which
631 could be attributed to the prolonged resident time facilitating following reactions.

632

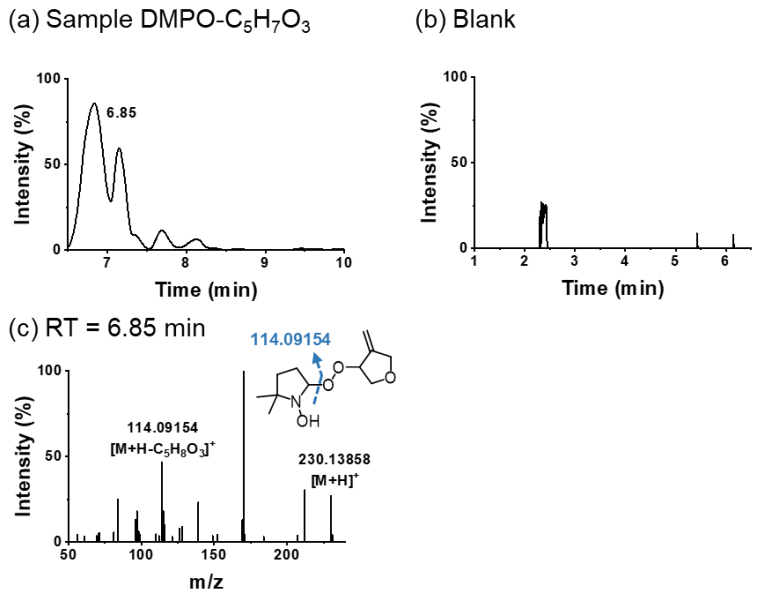

633

634 Figure S17. (a) The DMPO-adducted product of compound $C_5H_7O_3$ generated from OFR was
635 identified through comparison between sample (a) and process blank (b). The characteristic
636 [DMPO-$C_5H_7O_3$+2H] $^+$ ion (m/z = 230.14) eluted at 6.85 min was selected for MS/MS analysis.
637 The structures of the other peaks could not be inferred because of their low abundance which may
638 due to the low concentration of poor sensitivity. No visible DMPO-trapped products of compound
639 $C_5H_7O_3$ were detected in the calibration source experiments.

640

641

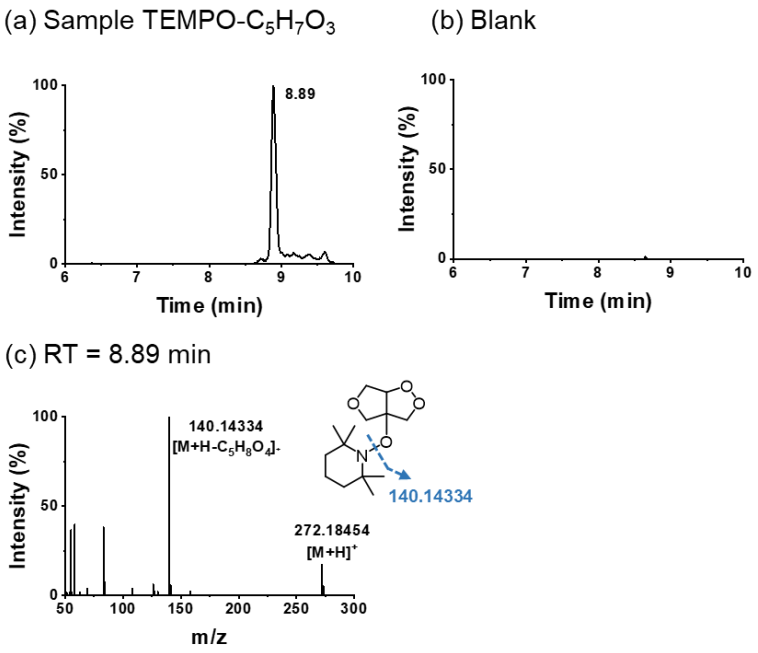

642

643 Figure S18. (a) The TEMPO-adducted product of compound $C_5H_7O_3$ from OFR was identified
644 through comparison between sample (a) and process blank (b). The characteristic [TEMPO-
645 $C_5H_7O_3$+H] $^+$ ion (m/z = 272.19) eluted at 8.89 min was selected for MS/MS analysis. The
646 structures of the other peaks could not be inferred because of their low abundance which may due
647 to the low concentration of poor sensitivity. No visible TEMPO-trapped products of compound
648 $C_5H_7O_3$ were detected in the calibration source experiments.

649

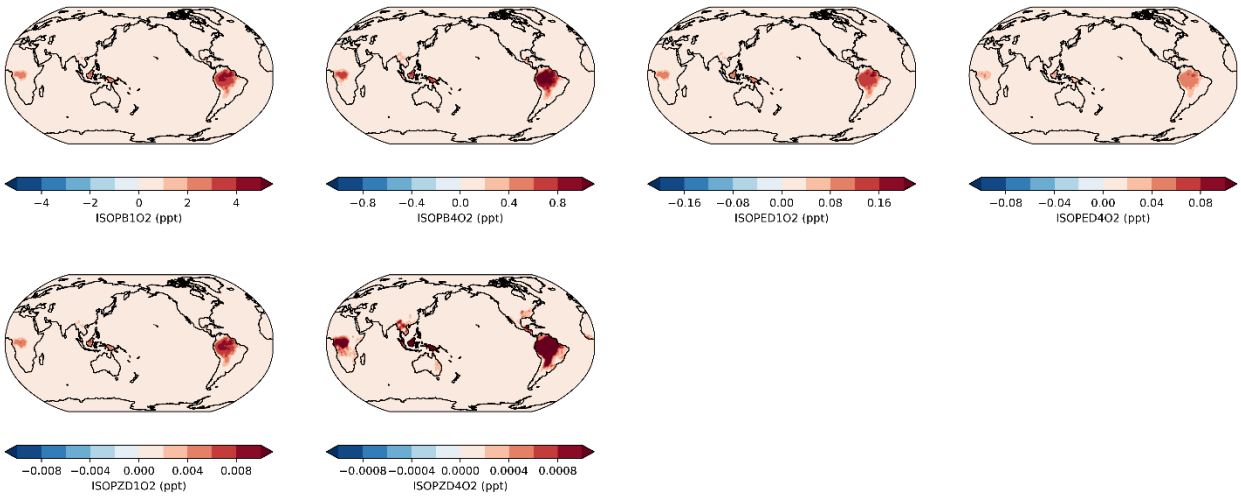

650

651 Figure S19. Spatial concentrations (in parts per trillion, ppt) of key isoprene-derived peroxyl
652 radicals in base model simulations. From top left to bottom right, species include: $ISOPB_1O_2$,
653 $ISOPB_4O_2$, $ISOPED_1O_2$, $ISOPED_4O_2$, $ISOPD_1O_2$ and $ISOPD_4O_2$ [98].

654

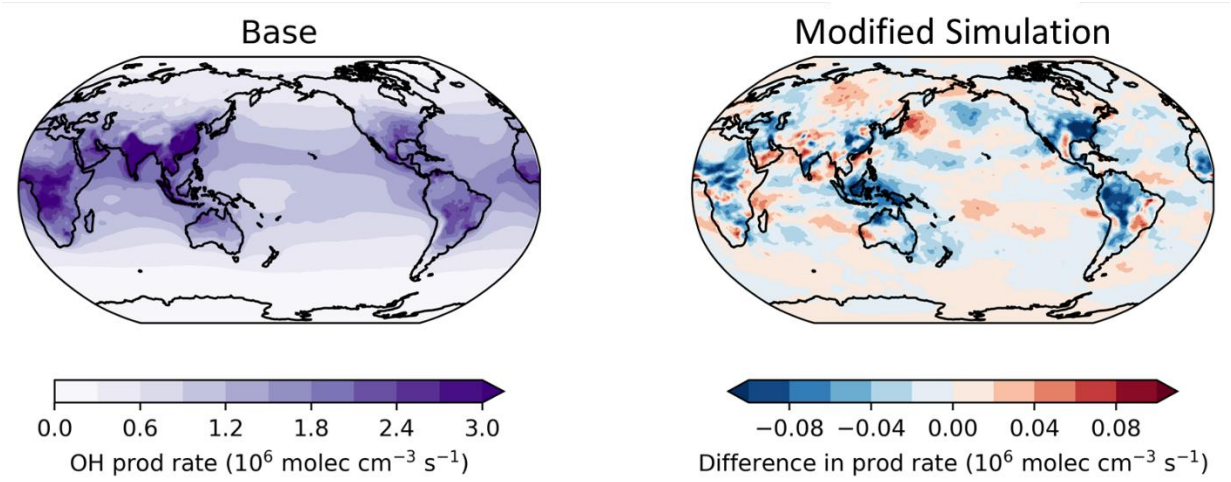

Figure S20. Global OH production rates and their differences between baseline and modified simulations. The left panel shows the simulated annual mean hydroxyl radical (OH) production rate (in 10^6 molecules cm^{-3} s^{-1}) for the baseline simulation, while the right panel displays the difference between the modified and baseline simulations. Blue areas in the difference map represent regions with reduced OH production, and red areas indicate increased production. Significant changes are observed over eastern China, the United States, and the Amazon, reflecting the impact of the newly modified branching ratio and pathway of H-abstraction mechanisms on atmospheric oxidizing capacity.

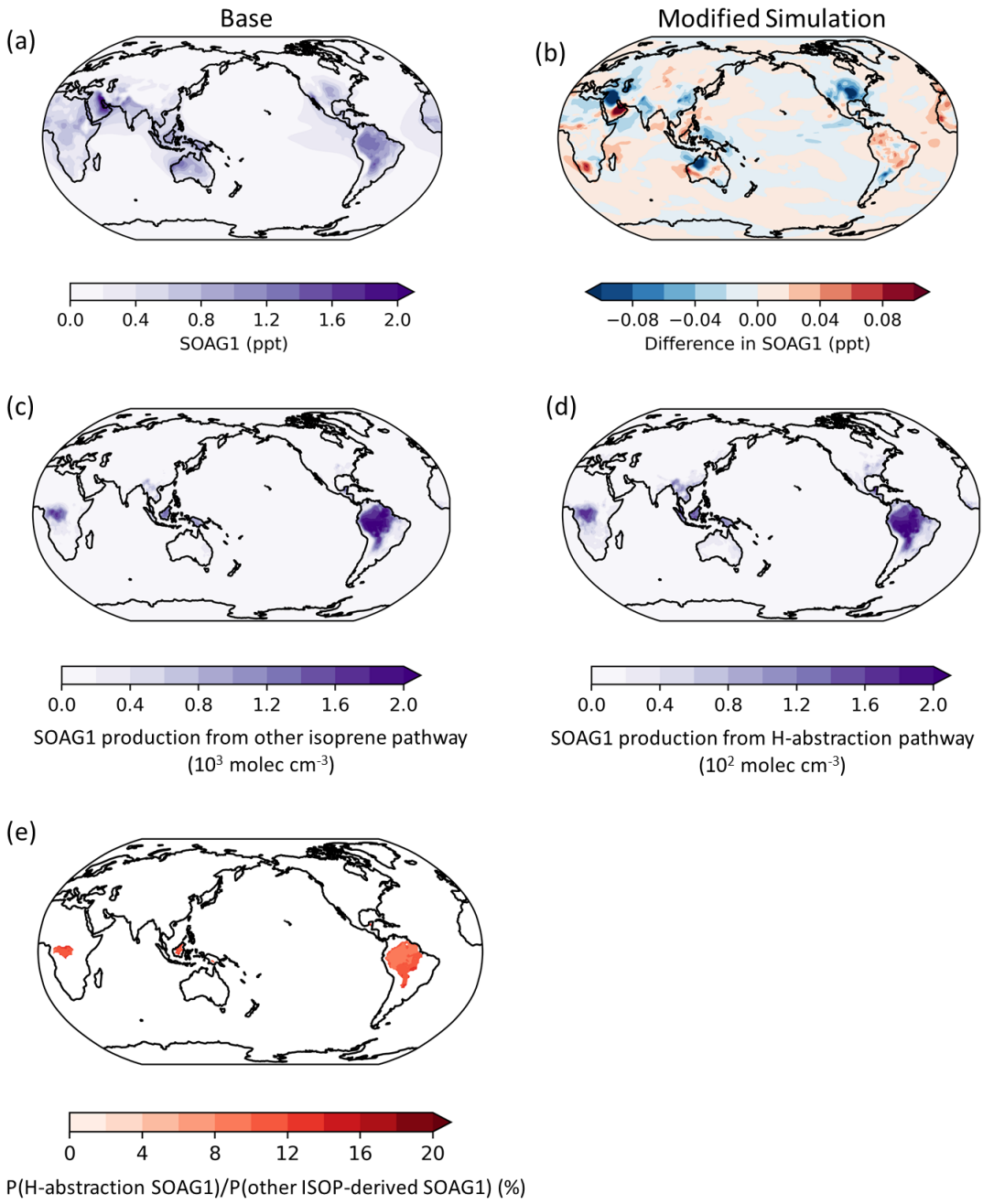

665

666 Figure S21. The source contributions of simulated low-volatility secondary organic aerosol
667 SOAG1 concentrations. (a) SOAG1 concentration (ppt). (b) Difference in SOAG1 concentration
668 in the modified simulation. (c) SOAG1 production from other isoprene-derived pathways exclude
669 H-abstraction pathway (10^3 molec cm^{-3}). (d) SOAG1 production attributed to hydrogen abstraction

pathway (10^3 molec cm^{-3}). (e) The ratio of these two production pathways' SOAG1 contribution (%). In BVOC abundant regions the ratio is 9.0 - 15.6% with a regional average value of 10.5%. The results highlight the potential contribution of SOA from the abstraction channel.

(a)

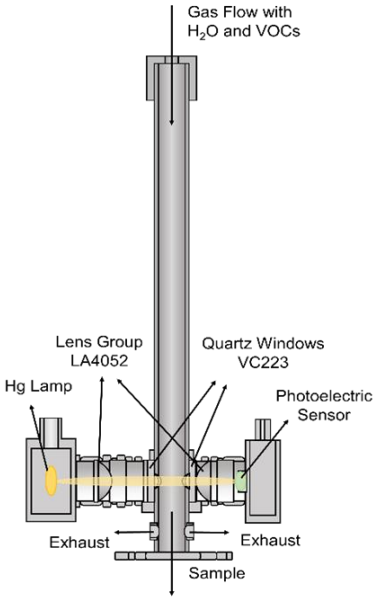

(b)

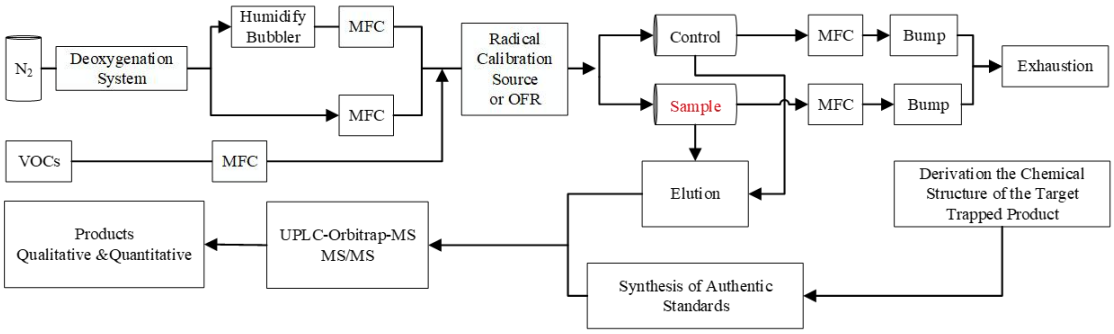

Figure S22. (a) Schematic of the custom-built radical calibration source used in the experiments. Target compounds are mixed with OH precursors and photolyzed in a reaction cell under controlled flow conditions. The system includes mass flow controllers (MFCs), a deoxygenation unit, and a UV photolysis source for OH generation. The resulting radicals are immediately

captured by spin-trapping agents (e.g., TEMPO, DMPO) on a solid-phase substrate. The adducts are subsequently eluted and analyzed via high-resolution mass spectrometry to provide reference spectra for compound identification and quantification. (b) Overview of the full experimental workflow for gas-phase radical detection in the OH-initiated oxidation of isoprene. The system integrates the radical generation reactor (e.g., oxidation flow reactor), radical capture using solid-phase substrates, and subsequent UHPLC–HRMS analysis. Trapping agents selectively stabilize reactive intermediates, enabling structural identification and quantification of short-lived radicals involved in the early-stage oxidation mechanisms.

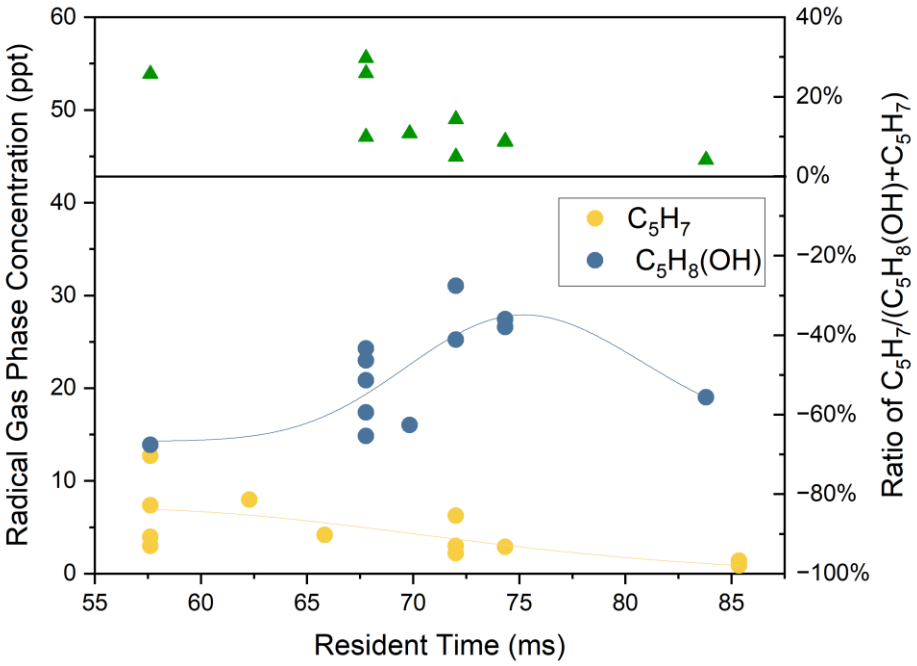

689

690 Figure S23. The concentration of •C_5H_7 increased with decreasing residence time (RT) shown in
691 the yellow dots and the concentration of •C_5H_8(OH) shown an insignificant upward and then
692 downward trend with RT as illustrated in blue dots. Their ratio decreases from 29.68% to 4.15%
693 as shown in the green triple dots. The presence of polar substituents (e.g., –OH, –COOH) increases
694 the polarity of the radical center and can enhance the cross-coupling reaction rate between a
695 nitroxide (such as TEMPO) and a C-centered radical. For •C_5H_7 radicals, the higher reaction rate
696 with O_2 compared to TEMPO may result in the absence of detectable TEMPO adduct signals in
697 this study. In contrast, spin traps such as DMPO and CHANT may exhibit higher trapping rates
698 with •C_5H_7 radicals, thereby facilitating their detection.

699

S3. Tables S1 to S6

Table S1. The quantum chemical calculations helped to assessed the contributions of cis- and trans-radicals to struc-8 and struc-9. All rate constant calculations k were performed using a Master Equation Solver for Multi Energy-well Reactions (MESMER) code [87].

Reaction rates (s^{-1})			
	1-OH Tc		4-OH Tc
1-OH cis	49249.55 (49.4%)	4-OH cis	47134.4 (51.7%)
1-OH trans	50380.45 (50.6%)	4-OH trans	44003.1 (48.3%)

Table S2. Summary of the newly implemented oxidation mechanism for the H-abstraction pathway, including product branching and rate constants. This mechanism incorporates hydrogen abstraction by OH and subsequent peroxyl radical chemistry.

Reaction	Rate
ISOP + OH→0.482 $ISOPC_1T$ + 0.163 $ISOPC_1C$ + 0.064 $ISOPC_4T$ + 0.203 $ISOPC_4C$ + 0.088 $ISOPC_1H$	2.70e-11 exp (390.00/t)
$ISOPC_1H + O_2 \rightarrow C_5H_7O_2$	1e-12
$C_5H_7O_2 \rightarrow C_5H_7O_6$	0.077
$C_5H_7O_6 + NO \rightarrow 0.0035\ SOAG_1$	1.1e-11
$C_5H_7O_6 \rightarrow HCHO + CO + HO_2 + C_3H_4O_4$	0.3
$C_3H_4O_4 \rightarrow SOAG_1$	3.5×10^{-3}
	$(8.2\times10^{-3}$ to $5.8\times10^{-5})$ [a]

[a] The reaction rate was calculated under the typical ambient conditions as 5 to 287 min [101] of glyoxal heterogenous reactions, with the aid of uptake coefficient as 0.0002 [98] to 0.0033 [92,102] with typical aerosol surface area as 3×10^{-4} cm^3/cm^3 and mean molecular speed as 3.3×10^4 cm/s. We assume that all glyoxal that is taken up by aerosol particles is irreversibly converted into SOA (i.e., 100% yield upon uptake), consistent with common treatments in global and regional chemical transport models (e.g., GEOS-Chem, MOZART, and CAM-Chem) [103].

Table S3. The mean wall loss rates and fractions of different species in the calibration source. We assumed that k_{wall2} played a role in the whole oxidant period which was in fact not true, the wall effect from the junction between the calibration source and the solid phase column inlet may only account for less than 10% period. The wall loss fractions are the upper limit.

Species	D_g ($cm^2\ s^{-1}$)	k_{wall1} (s^{-1})	k_{wall2} (s^{-1})	Production rate (molecule $cm^3\ s^{-1}$)	Wall loss rate (molecule $cm^3\ s^{-1}$)	Wall loss fraction
OH	0.23	0.047	0.960	1.12×10^{10}	8.59×10^{7}	0.77%
HO_2	0.15	0.038	0.626	5.95×10^{8}	3.37×10^{7}	5.66%
ISO-R	0.07 (estimated)	0.026	0.292	1.04×10^{10}	2.35×10^{8}	2.26%
ISO-RO_2	0.07	0.026	0.292	2.24×10^{9}	2.53×10^{7}	1.13%

Table S4. The wall loss rates and fractions of different species in the OFR. We assumed that k_{wall2} played a role in the whole oxidant period which was in fact not true, the wall effect from the junction between the calibration source and the solid phase column inlet may only account for less than 10% period. The wall loss fractions are the upper limit.

Species	D_g (cm^2 s^{-1})	k_{wall1} (s^{-1})	k_{wall2} (s^{-1})	Production rate (molecule cm^3 s^{-1})	Wall loss rate (molecule cm^3 s^{-1})	Wall loss fraction
OH	0.23	0.0050	0.960	9.05×10^{11}	1.62×10^{8}	0.017%
HO_2	0.15	0.0040	0.626	6.88×10^{11}	1.53×10^{10}	2.22%
R	0.07 (estimated)	0.0027	0.292	5.36×10^{11}	8.89×10^{8}	0.17%
RO_2	0.07	0.0027	0.292	5.48×10^{11}	2.46×10^{9}	0.45%

Table S5. Relative uncertainties in calibration-derived radical concentrations. The value of F×t is 1.08×10^{12}. The correlation equation of $[OH]_{count}$ with the concentration of OH is $[OH]=1.83\times10^{7}\times[OH]_{count}$, $R^2=0.997$. Thus, the correlation of RH with [OH] in the condition of low oxygen (<0.1ppm) and 20L/min flow is $[OH]=-6.12\times10^{6}\times RH^2+1.06\times10^{9}\times RH-3.60\times10^{9}$, $R^2=0.998$. The non-liner correlation between them is attributed to the interferences of water vapor on the photolysis and reaction with OH.

Parameter	Value	Uncertainty (1σ)
σ_{water}	7.1×10^{-20} cm^2	3%
φ_{OH+H}	1.0	<0.5%
$[O_2]$	6.75%	2.5%
$\sigma_{O_2}^{eff}$	1.63×10^{-20} cm^2	2%
RH	0.1-0.6	0.5%
Total		6.67%

Table S6. Tropospheric airmass-weighted concentrations of key oxidants, isoprene oxidation intermediates, and SOA-related species from global simulations. Columns report values from the base simulation, the modified simulation including the changing of branching ratio and addition of H-abstraction pathway, and the absolute difference between them. All values are airmass-weighted tropospheric averages; species marked as "new added" were absent from the base simulation. Units are in parts per trillion (ppt), except for SOA1, which is expressed in 10^{-11} kg per kg of air.

	Base	Modified	Difference
OH (ppt)	0.077	0.077	
HO_2 (ppt)	5.61	5.59	-0.02
IEPOX (ppt)	6.38	5.92	-0.47
Isoprene (ppt)	43.6	44.8	
SOAG1 (ppt)	0.19	0.19	
SOA1 (10^{-11} kg/kg)	6.97	6.94	
ISOPC1T (ppt)	2.5e-8	2.5e-8	
ISOPC1C (ppt)	4.6e-9	4.5e-9	

ISOPC4T (ppt)	1.4e-9	9.4e-10	
ISOPC4C (ppt)	7.0e-10	4.8e-10	
ISOPC1H (ppt), new added	N/A	2.5e-11	
$ISOPB_1O_2$ (ppt)	0.096	0.096	
$ISOPB_4O_2$ (ppt)	0.027	0.019	-0.008
$ISOPED_1O_2$ (ppt)	0.0039	0.0039	
$ISOPED_4O_2$ (ppt)	0.0015	0.00097	-0.0005
$ISOPZD_1O_2$ (ppt)	0.0002	0.0002	
$ISOPZD_4O_2$ (ppt)	6.7e-5	4.5e-5	-2.0e-5
$C_5H_7O_2$ (ppt), new added	N/A	0.0014	
$C_5H_7O_6$ (ppt), new added	N/A	0.0003	

RO_2 total (ppt)	0.128	0.121	-0.007

743

744

745

S4. Synthetic Procedures and Characterization Data and Figs. S24 to S28

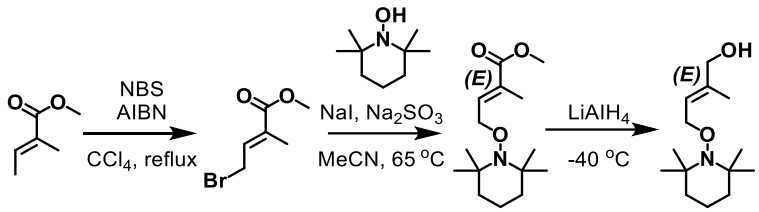

Scheme S1. Synthetic process of (E)-2-methyl-4-((2,2,6,6-tetramethylpiperidin-1-yl)oxy)but-2-en-1-ol (1-OH-TEMPO adducts).

(E)-2-methyl-4-((2,2,6,6-tetramethylpiperidin-1-yl)oxy)but-2-en-1-ol was prepared according to Scheme 1. To a stirred solution of methyl (E)-2-methylbut-2-enoate in CCl_4 was added NBS and a catalytic amount of AIBN. The mixture solution was heated to reflux and maintained for several hours. After the reaction was completed, the mixture solution was cooled to the room temperature, and filtered to remove the byproduct and to get methyl (E)-4-bromo-2-methylbut-2-enoate. The purified product from the previous step was dissolved in acetonitrile with NaI, Na_2SO_3, and TEMPO. The mixture solution was stirred at 65 °C for several hours and cooled to room temperature after the reaction was completed, and then, methyl (E)-2-methyl-4-((2,2,6,6-tetramethylpiperidin-1-yl)oxy)but-2-enoate was obtained. Finally, the purified product from the previous step was reacted with $LiAlH_4$ at -40 °C, and was reduced to obtain target compound.

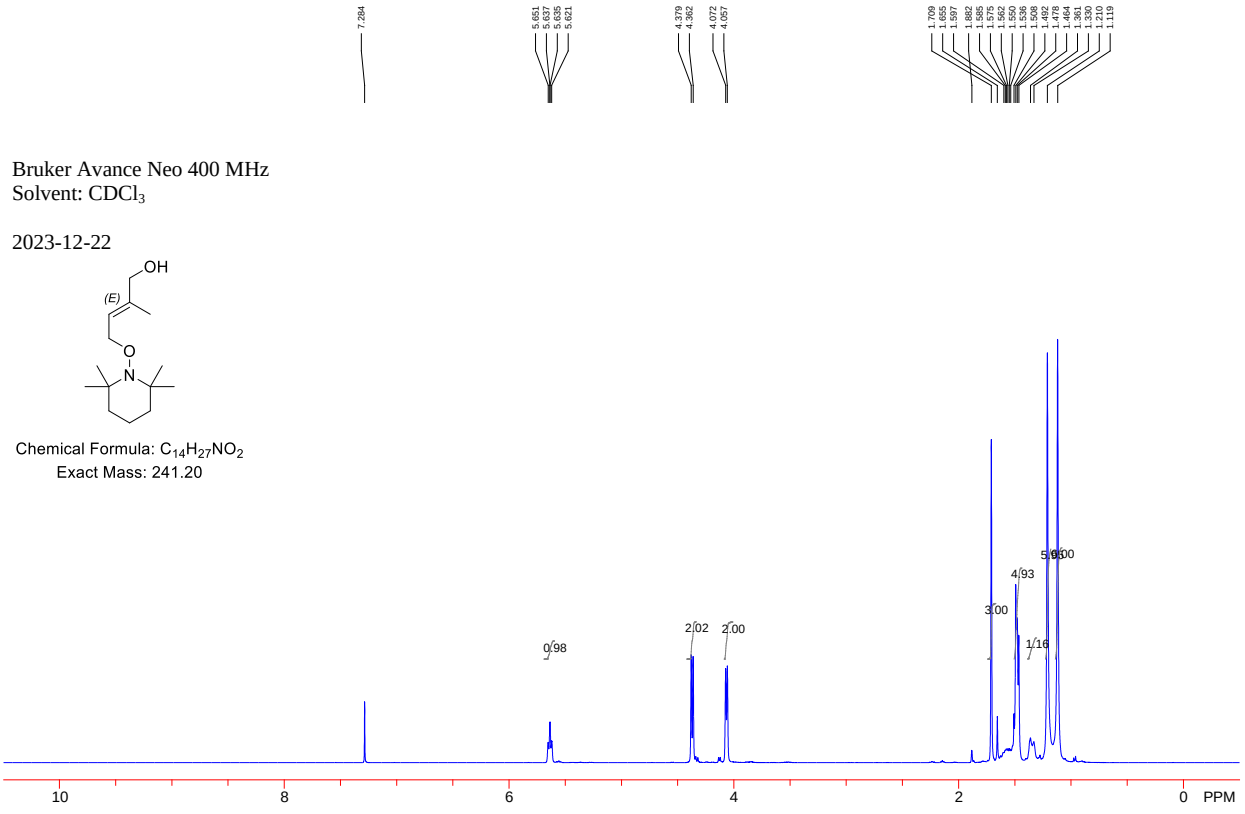

760

761 Figure. S24 The HRMS of 1-OH-TEMPO adducts.

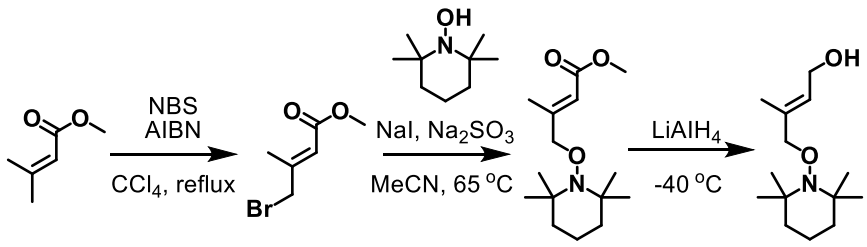

762

763 Scheme S2. (E)-3-methyl-4-((2,2,6,6-tetramethylpiperidin-1-yl)oxy)but-2-en-1-ol (4-OH-

764 TEMPO adducts)

765 (E)-3-methyl-4-((2,2,6,6-tetramethylpiperidin-1-yl)oxy)but-2-en-1-ol was obtained according

766 to Scheme 2. First, to a stirred solution of methyl 3-methylbut-2-enoate in CCl_4 was added NBS,

767 and AIBN, and the mixture solution was heated to reflux and maintained for several hours. Methyl

768 (E)-4-bromo-3-methylbut-2-enoate was obtained after reaction and purification, which was then

769 dissolved in MeCN with TEMPO, NaI, and Na_2SO_3, and heated to 65 °C. After cooling to room
770 temperature, methyl (E)-3-methyl-4-((2,2,6,6-tetramethylpiperidin-1-yl)oxy)but-2-enoate was
771 obtained. Finally, the product from the previous step was reduced by $LiAlH_4$ at -40 °C to get target
772 compound.

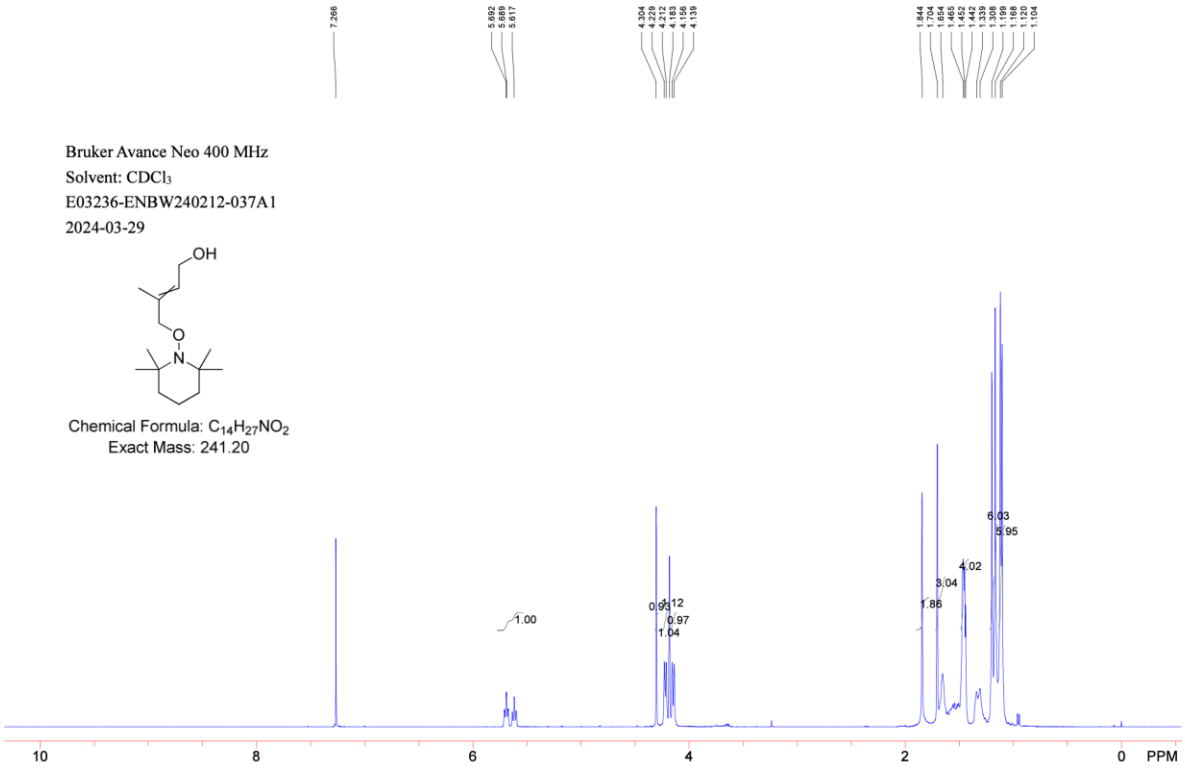

773

774 Figure S25 The HRMS of 4-OH-TEMPO adducts.

775

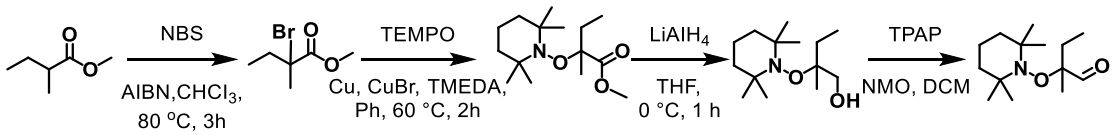

776

777 Scheme S3. 2-methyl-2-((2,2,6,6-tetramethylpiperidin-1-yl)oxy)butanal (Structure 7)

2-methyl-2-((2,2,6,6-tetramethylpiperidin-1-yl)oxy)butanal (Structure 7) was prepared according to Scheme 3. To a stirred solution of methyl 2-methylbutanoate in $CHCl_3$ was added NBS and a catalytic amount of AIBN. The mixture solution was stirred for 3 h at 80 °C. After the reaction was completed, the mixture solution was purified by silical gel column to get methyl 2-bromo-2-methylbutanoate, and the structure was confirmed by ^{1}H-NMR. Then, the product was dissolved in benzene with TEMPO, Cu, CuBr, and TMEDA and was stirred for 2 h at 60 °C to get methyl 2-methyl-2-((2,2,6,6-tetramethylpiperidin-1-yl)oxy)butanoate. After purification by silical gel column, the product and $LiAiH_4$ was added into THF and the reaction temperature was maintained at 0 °C for 1 h to get 2-methyl-2-((2,2,6,6-tetramethylpiperidin-1-yl)oxy)butan-1-ol. After purification, TPAP, NMO, and product from the previous step was dissolved in DCM to obtain the oxidation product, Structure 7. MS (ES, m/z): $[M+1]^+$ = 241.8. ^{1}H-NMR (400 MHz, DMSO-d_6): 9.713 (s, 1H), 1.945-1.935 (m, 2H), 1.773-1.706(m, 2H), 1.628-1.422 (m, 4H), 1.315 (s, 3H), 1.195 (s, 3H), 1.162 (s, 3H), 1.109 (s, 3H), 0.914 (s, 3H), 0.835 (t, 3H).

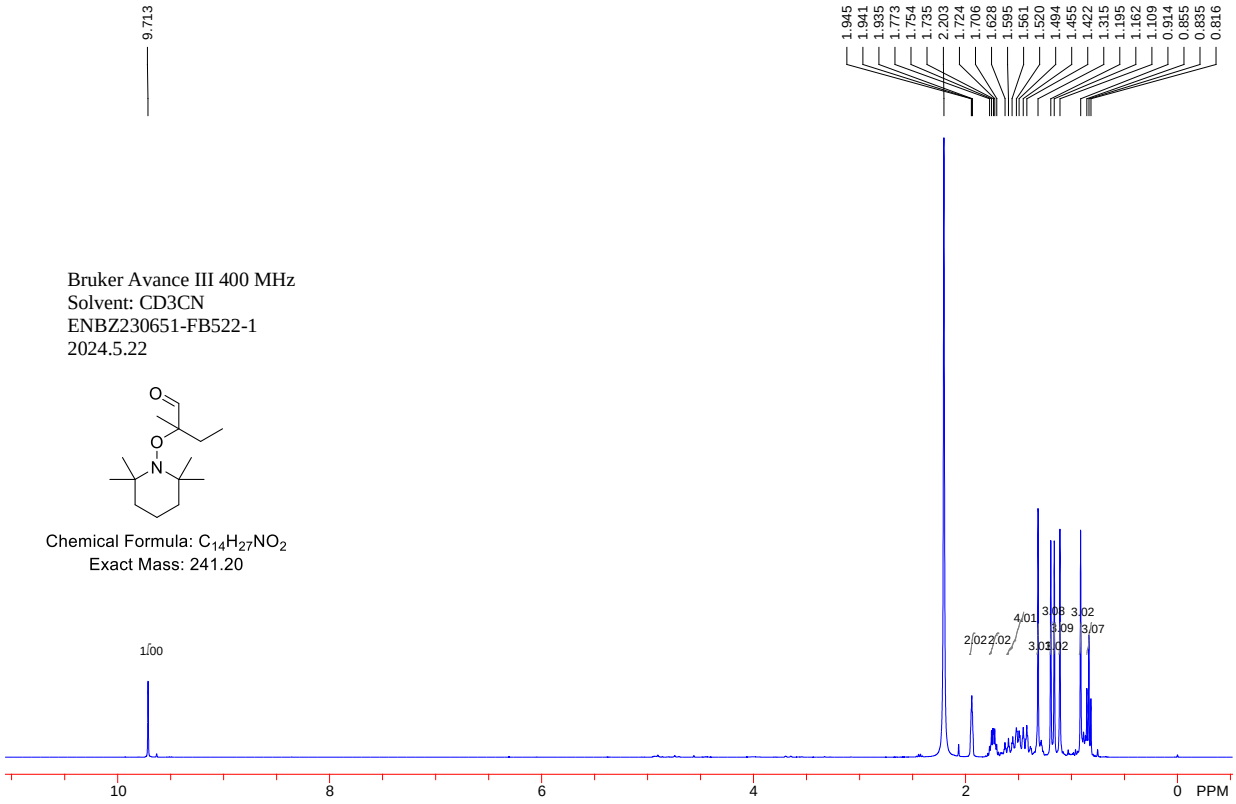

791

792 Figure S26. The HRMS of structure 7.

793

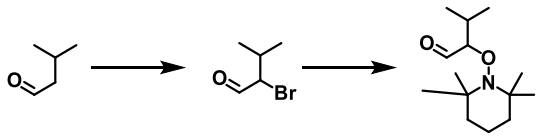

794

795 Scheme S4. 3-methyl-2-((2,2,6,6-tetramethylpiperidin-1-yl)oxy)butanal (Structure 11)

796 To a stirred solution of TEMPO (1 g, 6.40 mmol, 1.0 eq.) in MeCN (10.0 mL) was added
797 $Ru(bpy)_3(PF_6)_2$ (110 mg, 0.13 mmol, 0.02 eq.), morpholine (28 mg, 0.32 mmol, 1.0 eq.), 3-
798 methylbutanal (1.10 g, 12.80 mmol, 2.0 eq.) and stirred for 16 h under 435nm blue LED. The
799 mixture was purified by reverse column (MeCN : NH_4HCO_3=0 to 100%) to give **Structure 11**

(150 mg, 9.74%) as a pale yellow liquid. MS (ES, m/z): $[M+1]^+$ = 241.8. ^{1}H-NMR (400 MHz, DMSO-d_6): 9.853 (d, *J*=5.2Hz, 1H), 3.868-3.838 (m, 1H), 2.175-2.089 (m, 1H), 1.563-1.325 (m, 6H), 1.169 (s, 12H), 1.039 (d, *J*=6.8Hz, 3H), 0.951 (d, *J*=6.8Hz, 3H).

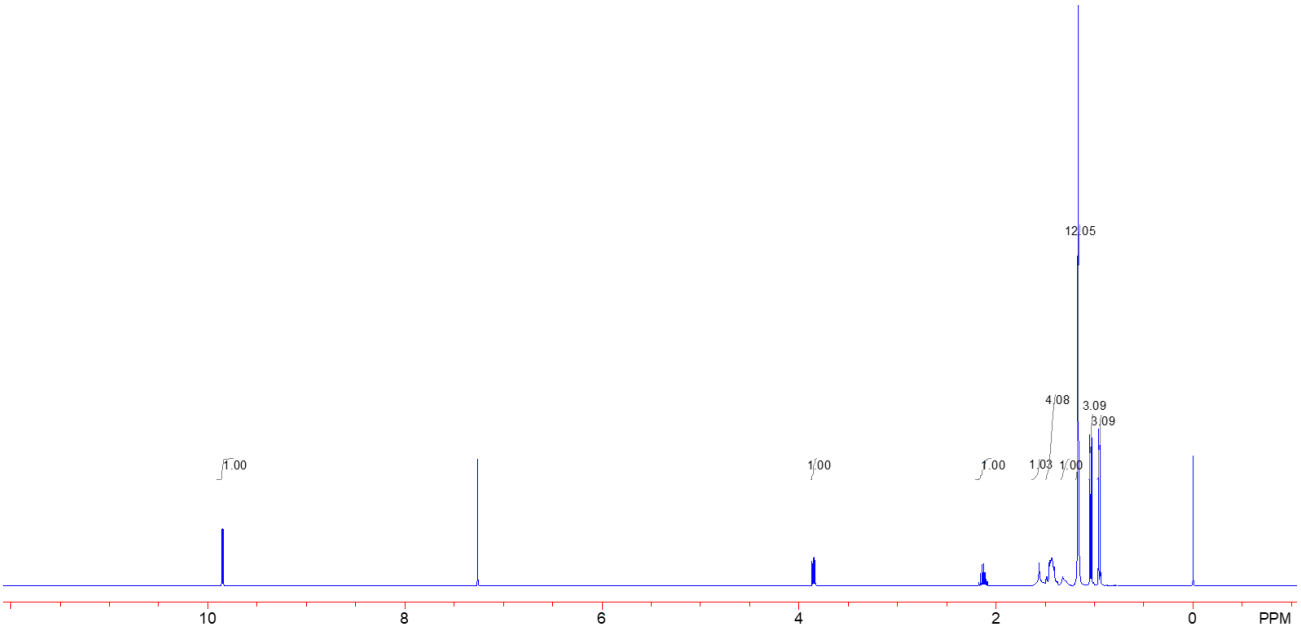

Figure S27. The HRMS of structure 11.

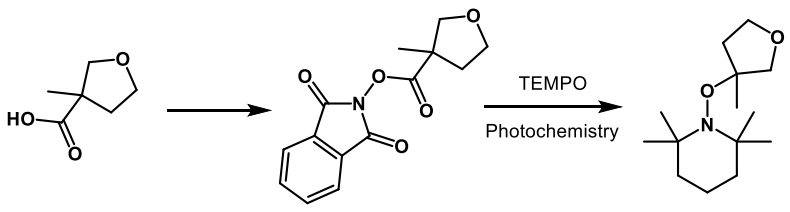

Scheme S5. 2,2,6,6-tetramethyl-1-((3-methyltetrahydrofuran-3-yl)oxy)piperidine (Structure 10)

2,2,6,6-tetramethyl-1-((3-methyltetrahydrofuran-3-yl)oxy)piperidine (Structure 10) was obtained from Scheme 5. First, 3-methyltetrahydrofuran-3-carboxylic acid was reacted with 2-hydroxyisoindoline-1,3-dione. Then, 1,3-dioxoisoindolin-2-yl 3-methyltetrahydrofuran-3-carboxylate was obtained, which was then mixed with TEMPO. Finally, after a photochemical reaction occurred, Structure 10 was finally obtained.

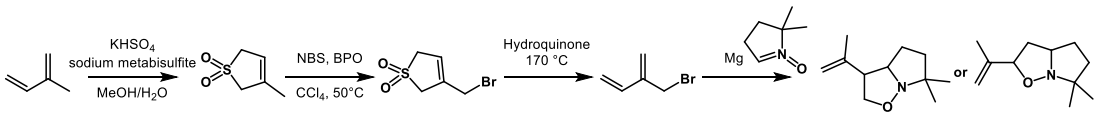

Scheme S6. 6,6-dimethyl-3-(prop-1-en-2-yl)hexahydropyrrolo[1,2-b]isoxazole or 6,6-dimethyl-2-(prop-1-en-2-yl)hexahydropyrrolo[1,2-b]isoxazole

To a solution of 1 (5 g, 0.073 mol) in methanol (146 mL) and water (40 mL) was added $KHSO_4$ (20 g, 0.146 mol) and sodium metabisulfite (70 g, 0.365 mol). The reaction mixture was stirred at 100 °C for 14 h under N_2. The reaction mixture was cooled to room temperature and concentrated. The solution was extracted with EA (100 mL, 3 times). The combined organic layers were dried over anhydrous Na_2SO_4 and concentrated under reduced pressure to afford the product (2.5 g, yield 25.7%). To a solution of 2 (22 g, 166 mmol) in chloroform (250 mL) was added NBS (35.4 g, 199 mmol) and BPO (2 g, 8.3 mmol). The reaction mixture was stirred at 75 °C for 16 h under N_2. The reaction mixture was poured into water (500 mL) and extracted with DCM (100 mL, 3 times). The combined organic layers were washed with water (100 mL) and brine (100 mL), dried over Na_2SO_4 and concentrated to give crude product. The crude product was purified by silica gel chromatography (PE/EA=20/1~5/1) to give product (11 g, yield 31.2%). A 50 mL round-bottom flask was charged with (5 g, 23.6 mmol) of 3-bromomethyl-2,5-dihydrothiophene-1,1-dioxide and

about 20 mg of hydroquinone, and connected to a condenser with a receiving flask. The round-bottom flask was then placed in a pre-heated oil bath at 170 °C. After the solid had melted, vacuum was applied with a water aspirator. Sulfur dioxide was evolved and the product was collected in the receiving flask cooled in an ice bath to give product (2 g, yield 57%). To a solution of Mg (0.2 g, 8.3 mmol) in THF (5 mL) was added 4 (0.6 g, 4.08 mmol) in THF (2 mL) dropwise at 30 °C. The reaction mixture was stirred at 30 °C for 1 h under N_2. Then DMPO (565 mg, 5.0 mmol) was added dropwise at 30 °C. Then the mixture was stirred at 50 °C for 5 h. The solution was poured into water (20 mL) and extracted with DCM (30 mL, 3 times). The combined organic layers were dried over Na_2SO_4 and concentrated to give crude product. The crude product was purified by prep-HPLC.

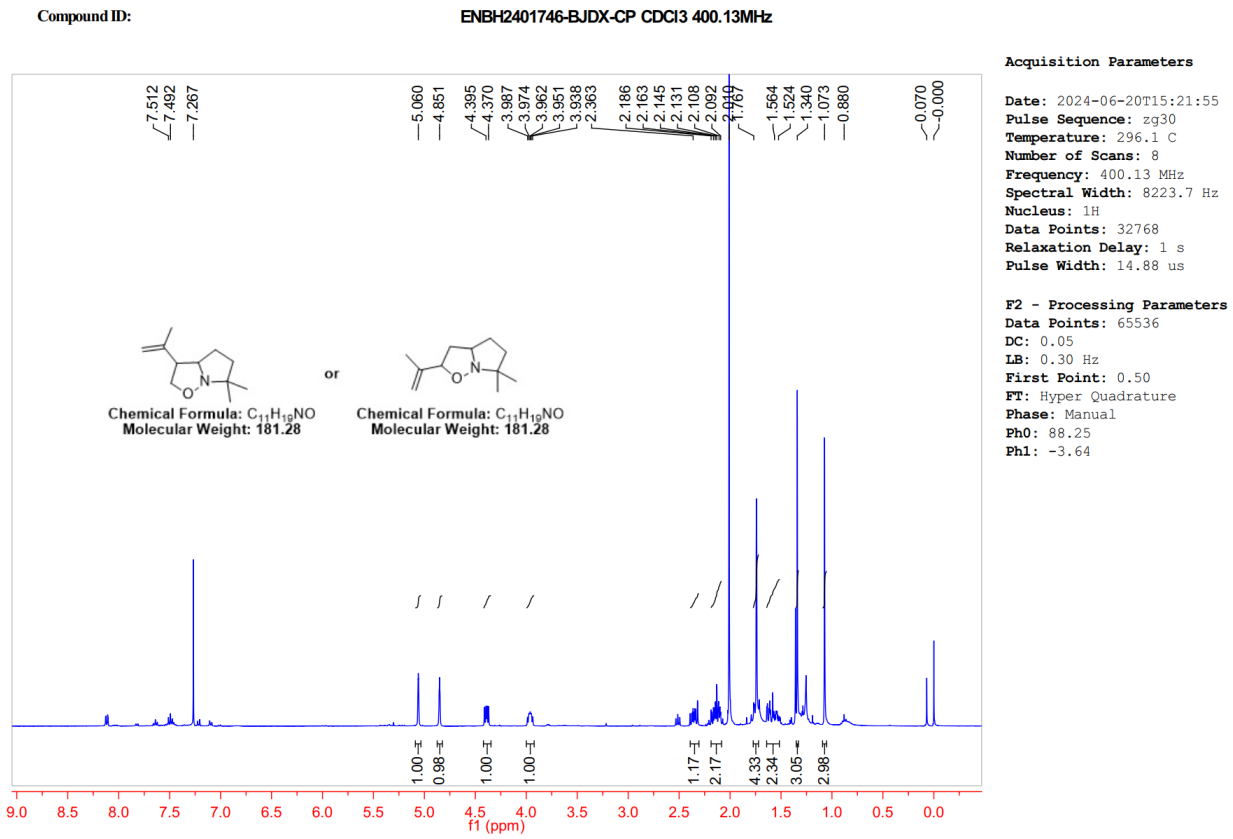

Figure S28. The HRMS of 6,6-dimethyl-3-(prop-1-en-2-yl)hexahydropyrrolo[1,2-b]isoxazole.

References

70 Williams, P. J. H. *et al.* New Approach to the Detection of Short-Lived Radical Intermediates. *Journal of the American Chemical Society* **144**, 15969-15976 (2022). https://doi.org:10.1021/jacs.2c03618

71 Kanaya, Y., Sadanaga, Y., Hirokawa, J., Kajii, Y. & Akimoto, H. Development of a ground-based LIF instrument for measuring HOx radicals: Instrumentation and calibrations. *J Atmos Chem* **38**, 73-110 (2001). https://doi.org:Doi 10.1023/A:1026559321911

72 Wang, F. *et al.* Development of a field system for measurement of tropospheric OH radical using laser-induced fluorescence technique. *Optics Express* **27**, A419-A435 (2019).

73 Heard, D. E. & Pilling, M. J. Measurement of OH and HO_2 in the troposphere. *Chemical Reviews* **103**, 5163-5198 (2003). https://doi.org:10.1021/cr020522s

74 Cantrell, C. A., Zimmer, A. & Tyndall, G. S. Absorption cross sections for water vapor from 183 to 193 nm. *Geophysical Research Letters* **24**, 2195-2198 (1997).

75 Creasey, D. J., Heard, D. E. & Lee, J. D. Absorption cross-section measurements of water vapour and oxygen at 185 nm. Implications for the calibration of field instruments to measure OH, HO2 and RO2 radicals. *Geophysical Research Letters* **27**, 1651-1654 (2000).

76 Palm, B. B. *et al.* In situ secondary organic aerosol formation from ambient pine forest air using an oxidation flow reactor. *Atmospheric Chemistry and Physics* **16**, 2943-2970 (2016).

77 Tang, M., Cox, R. & Kalberer, M. Compilation and evaluation of gas phase diffusion coefficients of reactive trace gases in the atmosphere: volume 1. Inorganic compounds. *Atmospheric Chemistry and Physics* **14**, 9233-9247 (2014).

78 Hansel, A., Scholz, W., Mentler, B., Fischer, L. & Berndt, T. Detection of RO2 radicals and other products from cyclohexene ozonolysis with NH4+ and acetate chemical ionization mass spectrometry. *Atmospheric Environment* **186**, 248-255 (2018).

79 Huang, Y. *et al.* Unified theory of vapor–wall mass transport in Teflon-walled environmental chambers. *Environmental science & technology* **52**, 2134-2142 (2018).

80 Peng, Z. & Jimenez, J. L. Radical chemistry in oxidation flow reactors for atmospheric chemistry research. *Chemical Society Reviews* **49**, 2570-2616 (2020).

81 Davis, D. D., Ravishankara, A. R. & Fischer, S. SO2 oxidation via the hydroxyl radical: Atmospheric fate of HSOx radicals. *Geophysical Research Letters* **6**, 113-116 (1979). https://doi.org:https://doi.org/10.1029/GL006i002p00113

82 Mao, J. *et al.* Airborne measurement of OH reactivity during INTEX-B. *Atmospheric Chemistry and Physics* **9**, 163-173 (2009). https://doi.org:10.5194/acp-9-163-2009

83 Jenkin, M., Young, J. & Rickard, A. The MCM v3. 3.1 degradation scheme for isoprene. *Atmospheric Chemistry and Physics* **15**, 11433-11459 (2015).

84 Ma, F. *et al.* Atmospheric Chemistry of Allylic Radicals from Isoprene: A Successive Cyclization-Driven Autoxidation Mechanism. *Environmental Science & Technology* **55**, 4399-4409 (2021). https://doi.org:10.1021/acs.est.0c07925

85 Atkinson, R. Rate constants for the atmospheric reactions of alkoxy radicals: An updated estimation method. *Atmospheric Environment* **41**, 8468-8485 (2007).

86 Frisch, M. e. *et al.* (Gaussian, Inc. Wallingford, CT, 2016).

87 Glowacki, D. R., Liang, C.-H., Morley, C., Pilling, M. J. & Robertson, S. H. MESMER: an open-source master equation solver for multi-energy well reactions. *The Journal of Physical Chemistry A* **116**, 9545-9560 (2012).

88 Georgievskii, Y. & Klippenstein, S. J. Variable reaction coordinate transition state theory: Analytic results and application to the $C_2H_3 + H \rightarrow C_2H_4$ reaction. *The Journal of chemical physics* **118**, 5442-5455 (2003).

89 Horváth, G., Horváth, I., Almousa, S. A.-D. & Telek, M. Numerical inverse Laplace transformation using concentrated matrix exponential distributions. *Performance Evaluation* **137**, 102067 (2020).
90 Carr, S. A. *et al.* Experimental and Modeling Studies of the Pressure and Temperature Dependences of the Kinetics and the OH Yields in the Acetyl+O_2 Reaction. *The Journal of Physical Chemistry A* **115**, 1069-1085 (2011).
91 Maranzana, A., Barker, J. R. & Tonachini, G. Master equation simulations of competing unimolecular and bimolecular reactions: application to OH production in the reaction of acetyl radical with O_2. *Physical Chemistry Chemical Physics* **9**, 4129-4141 (2007).
92 Tilmes, S. *et al.* Climate forcing and trends of organic aerosols in the Community Earth System Model (CESM2). *Journal of Advances in Modeling Earth Systems* **11**, 4323-4351 (2019).
93 Emmons, L. K. *et al.* The Chemistry Mechanism in the Community Earth System Model Version 2 (CESM2). *Journal of Advances in Modeling Earth Systems* **12**, e2019MS001882 (2020). https://doi.org:https://doi.org/10.1029/2019MS001882
94 Van Marle, M. J. *et al.* Historic global biomass burning emissions for CMIP6 (BB4CMIP) based on merging satellite observations with proxies and fire models (1750–2015). *Geoscientific Model Development* **10**, 3329-3357 (2017).
95 Hoesly, R. M. *et al.* Historical (1750–2014) anthropogenic emissions of reactive gases and aerosols from the Community Emissions Data System (CEDS). *Geoscientific Model Development* **11**, 369-408 (2018).
96 Feng, L. *et al.* The generation of gridded emissions data for CMIP6. *Geoscientific Model Development* **13**, 461-482 (2020).
97 Guenther, A. *et al.* The Model of Emissions of Gases and Aerosols from Nature version 2.1 (MEGAN2. 1): an extended and updated framework for modeling biogenic emissions. *Geoscientific Model Development* **5**, 1471-1492 (2012).
98 Schwantes, R. H. *et al.* Comprehensive isoprene and terpene gas-phase chemistry improves simulated surface ozone in the southeastern US. *Atmos. Chem. Phys.* **20**, 3739-3776 (2020). https://doi.org:10.5194/acp-20-3739-2020
99 Gerritz, L., Perraud, V., Weber, K. M., Shiraiwa, M. & Nizkorodov, S. A. Application of UHPLC-ESI-MS/MS to Identify Free Radicals via Spin Trapping with BMPO. *The Journal of Physical Chemistry A* **128**, 10240-10249 (2024). https://doi.org:10.1021/acs.jpca.4c05311
100 Bauer, N. A., Hoque, E., Wolf, M., Kleigrewe, K. & Hofmann, T. Detection of the formyl radical by EPR spin-trapping and mass spectrometry. *Free Radical Biology and Medicine* **116**, 129-133 (2018).
101 Liggio, J., Li, S.-M. & McLaren, R. Reactive uptake of glyoxal by particulate matter. *Journal of Geophysical Research: Atmospheres* **110** (2005). https://doi.org:https://doi.org/10.1029/2004JD005113
102 Knote, C. *et al.* Simulation of semi-explicit mechanisms of SOA formation from glyoxal in aerosol in a 3-D model. *Atmospheric Chemistry and Physics* **14**, 6213-6239 (2014).
103 Fu, T.-M. *et al.* Global budgets of atmospheric glyoxal and methylglyoxal, and implications for formation of secondary organic aerosols. *Journal of Geophysical Research: Atmospheres* **113** (2008). https://doi.org:https://doi.org/10.1029/2007JD009505